Metamorphic facies evolution and distribution in the Western Alps predicted by petrological-thermomechanical models

Joshua David Vaughan Hammon[1], Lorenzo Giuseppe Candioti[2], Thibault Duretz[3], and Stefan Markus Schmalholz[1]

[1]University of Lausanne
[2]UNIL Lausanne
[3]Universite de Rennes 1

November 23, 2022

Abstract

The evolution and distribution of metamorphic rocks throughout the western European Alps is indicative of subduction-related metamorphism. The present-day distribution of metamorphic rocks in the Western Alps exhibits a regional trend, with an internal high-pressure domain and decreasing grade towards the foreland. However, the processes by which high-grade continental rocks are formed and exhumed, as well as the evolution of the metamorphic architecture remains unclear. Here, we present a two-dimensional petrological-thermomechanical model to investigate the evolution and distribution of metamorphic facies within an orogenic wedge formed by subduction and continental collision. The model simulates an entire geodynamic cycle of extension, with passive margin formation and mantle exhumation, followed by thermal equilibration without applied far-field deformation, convergence, with subduction initiation, basin closure and collision. After thermal equilibration, we consider ad-hoc the serpentinization of the exhumed mantle. Models developing a weak subduction interface, due to 6 km serpentinite thickness, display a laterally varying peak metamorphic facies distribution, with the highest grade rocks within the core of the orogeny, agreeing with distributions in the Western Alps. In contrast, models with a stronger subduction interface (3 km serpentinite thickness) develop an orogenic wedge with a vertical metamorphic gradient. The metamorphic distribution is calculated using the peak P and T values of 10'000 numerical markers during their modelled P-T trajectories. The models indicate, during overall convergence, local extensional tectonics between the exhuming material and overriding plate, whereby the upper-plate hanging-wall is unroofed, moving with a normal sense of shear relative to the exhuming high-pressure rocks.

Metamorphic facies evolution and distribution in the Western Alps predicted by petrological–thermomechanical models

Joshua D. Vaughan-Hammon[1], Lorenzo G. Candioti[1], Thibault Duretz[2], Stefan M. Schmalholz[1]

[1]Institut des sciences de la Terre, Bâtiment Géopolis, Quartier UNIL-Mouline, Université de Lausanne, 1015 Lausanne (VD), Switzerland
[2]Univ Rennes, CNRS, Géosciences Rennes UMR 6118, Rennes, France

Key Points:

- Petrological–thermomechanical model predicts metamorphic facies distribution using 10'000 numerical markers.
- Metamorphic architecture of the Western Alps, including gradient and abundance, is reproduced.
- Weak plate interface controlled by serpentinite abundance is vital for extrusion-type exhumation of high-grade metamorphic facies rocks.

Corresponding author: Joshua D. Vaughan-Hammon, `Joshua.Vaughan-Hammon@unil.ch`

Abstract

The evolution and distribution of metamorphic rocks throughout the western European Alps is indicative of subduction-related metamorphism. The present-day distribution of metamorphic rocks in the Western Alps exhibits a regional trend, with an internal high-pressure domain and decreasing grade towards the foreland. However, the processes by which high-grade continental rocks are formed and exhumed, as well as the evolution of the metamorphic architecture remains unclear. Here, we present a two-dimensional petrological–thermomechanical model to investigate the evolution and distribution of metamorphic facies within an orogenic wedge formed by subduction and continental collision.

The model simulates an entire geodynamic cycle of extension, with passive margin formation and mantle exhumation, followed by thermal equilibration without applied far-field deformation, convergence, with subduction initiation, basin closure and collision. After thermal equilibration, we consider ad-hoc the serpentinization of the exhumed mantle. Models developing a weak subduction interface, due to 6 km serpentinite thickness, display a laterally varying peak metamorphic facies distribution, with the highest grade rocks within the core of the orogeny, agreeing with distributions in the Western Alps. In contrast, models with a stronger subduction interface (3 km serpentinite thickness) develop an orogenic wedge with a vertical metamorphic gradient. The metamorphic distribution is calculated using the peak P and T values of 10'000 numerical markers during their modelled P-T trajectories. The models indicate, during overall convergence, local extensional tectonics between the exhuming material and overriding plate, whereby the upper-plate hanging-wall is unroofed, moving with a normal sense of shear relative to the exhuming high-pressure rocks.

Plain Language Summary

Evidence for deep geological processes (>70 km) can be found in places throughout the Earth whereby plates have collided, subducted and then exhumed. Spectacular examples of this mountain building process can be seen in the European Alps. The pattern of mineral changes due to pressure and temperature conditions (metamorphic facies) exotic to crustal rocks who were once near the surface can be observed where the rocks who experienced the most extreme conditions are closest to the collision front. This study presents computer simulated models based on fundamental laws of physics and natural observations, that predict the large-scale metamorphic facies architecture preserved throughout the western European Alps.

1 Introduction

Since the observation of regional-scale systematic changes in index minerals (Barrow, 1893), the subsequent conceptualization of metamorphic facies (Eskola, 1915) and the introduction and acceptance of plate tectonics (Isacks et al., 1968; Le Pichon, 1968; Morgan, 1968), the dynamic nature of the Earth's crust has become a more clearer picture. More specifically, areas of crustal convergence, forming extensive mountain belts such as the European Alps, are observed to have unique metamorphic facies sequences linked to specific tectonic processes (Miyashiro, 2012). High-grade rocks exhumed in mountain belts, such as the European Alps, provide an ideal place to reconstruct and study deep tectono-metamorphic processes and subduction interface dynamics. In the European Alps, the distribution of metamorphic facies allows to identify (i) the spatial distribution of exhumed rocks that have been metamorphosed under similar pressure and temperature conditions (Bousquet et al., 2008; Frey et al., 1999; Lardeaux, 2014), (ii) the assessment of the ancient subduction direction (Ernst, 1971), and (iii) the spatial evolution of metamorphism through time (e.g. Lardeaux, 2014).

Advancements in dating metamorphism, in thermodynamic data and methods, in deterministic modelling based on fundamental laws of physics as well as the vast number of field and geophysical studies, has improved our understanding of the tectono-metamorphic evolution of the European Alps. Nevertheless, questions remain open regarding the transient conditions recorded in exhumed metamorphic terranes. These questions primarily concern: 1) temperature evolution with potentially episodic heating events, such as Barrovian metamorphism in the Lepontine dome (Berger et al., 2011; Burg & Gerya, 2005; Jamieson et al., 1998; Ryan & Dewey, 2019; Stüwe, 1998), which is vital for reconstructing paleo-geotherms during orogenesis, and 2) pressure evolution with potential local deviations from lithostatic pressure (Luisier et al., 2019; Schenker et al., 2015; Vaughan-Hammon et al., 2021), which is essential for reconstructing the vertical movement of rocks during orogenesis. Particularly, the mechanisms by which, often small volumes, of the highest grade, high-pressure and (ultra) high-pressure (HP + (U)HP), rocks are exhumed remain currently elusive (Beltrando, Compagnoni, & Lombardo, 2010; Chopin, 1987; Escher & Beaumont, 1997; Hacker & Gerya, 2013; Kurz & Froitzheim, 2002; Reinecke, 1991; Warren, 2013).

Petrologically-inspired burial and exhumation cycles of rocks within the Alps as well as their distribution through time and space, provides ample resources to test the validity of the tectono-metamorphic evolution predicted by deterministic numerical models. Here, we present a petrological–thermomechanical numerical model for subduction and syn-convergent exhumation of continental rocks. The numerical model is based on fundamental laws of physics and constrained by laboratory and field data that are directly applicable to the tectono-metamorphic evolution of the European Alps. The evolution of pressure and temperature for large portions of the continental rocks that are subducted and exhumed are traced through space and time, which enables metamorphic facies to be mapped within the modelled orogen. We analyse *c.* 10'000 numerical markers (out of *c.* 56 million markers in total) for each simulation, which store the evolution of pressure and temperature during convergence and we use them to generate cross-sections showing the metamorphic facies evolution and distribution, which we compare to published metamorphic facies distributions. We compare the role of inheritance, namely in the degree of serpentinization of the exhumed mantle separating the hyper-extended margins exposed during rifting and prior to collision, on the spatio-temporal distribution of metamorphic facies comprising exhuming continental rocks.

2 Tectono-metamorphic evolution of the Western Alps

The present-day large-scale tectonic architecture of the Western Alps derives from the convergence and ultimate collision of the formerly hyper-extended margins of the northern Adriatic continent and southern European continent (Figure 1). Subduction presumably started in the distal parts of the Adriatic margin and persisted from the late-Cretaceous (85–65 Ma, Sesia-Lanzo zone: Duchêne et al., 1997; Engi et al., 2011; Inger et al., 1996; Rubatto et al., 1999; Manzotti, Ballevre, et al., 2014) to the late-Eocene (35–32 Ma, Dora Maira: Tilton et al., 1989; Duchêne et al., 1997; Gebauer et al., 1997; Di Vincenzo et al., 2006). Later-stage folding events (40–25 Ma, Mischabel folding: Keller et al., 2005; Barnicoat et al., 1995) combined with earlier subduction related nappe emplacement resulted in the current tectonic configuration (Figure 1b), which can be constructed in section due to the strong Alpine topography, axial plunges of exhumed units and interpretation of high resolution seismic data (Escher & Beaumont, 1997; Escher et al., 1993; S. Schmid & Kissling, 2000; S. M. Schmid et al., 2017; Steck et al., 2015; Malusà et al., 2021). Paleogeographic reconstructions (e.g. Trümpy, 1975; S. M. Schmid et al., 2004; Lemoine et al., 1986; De Graciansky et al., 2011; McCarthy et al., 2020; Dal Piaz et al., 2001; Steck et al., 2015) of the Western Alps define 5 main domains (Figure 1a): 1) the structurally highest Adriatic margin comprising of the Ivrea Zone and Sesia- Dent Blanche continental units presumably separated by the exhumed sub-lithospheric mantle (e.g. Lanzo peridotites) from the main Adriatic margin, 2) the Piedmont oceanic domain separating Adria and Europe (e.g. Zermatt-Saas ophiolites), 3) Inner Penninic domain (e.g. Monte Rosa and Siviez-Mischabel), 4) Valais Zone of sub-lithospheric mantle (e.g. Monte Leone peridotites), and 5) the external Jura-Helvetic domains comprising external crystalline basement massifs (e.g. Mont Blanc) and sedimentary cover series (e.g. Morcles nappe).

The arcuate nature of the Western and central Alpine mountain belt has resulted in a metamorphic zoning pattern of similar geometry (Figure 2a). Throughout the western Alps, all metamorphic facies conditions are observed related to subduction, from (U)HP to greenschist facies (Figure 2a and b) (Oberhänsli et al., 2004; Bousquet et al., 2008). A first overview of the mineralogy and distribution of metamorphic indicators was provided in the 26th international Geol. Congress (Saliot, 1973), although (U)HP rocks were not identified until a few years after (e.g. Chopin, 1984). Soon after it was becoming more apparent that there exists a regional metamorphic trend, with an internal zone of high-pressure domains and decreasing metamorphic grade towards the external, foreland basin direction (Figure 2a, c and d).

Figure 2 shows a simplified metamorphic distribution of rocks within the Western Alps, modified after Oberhänsli et al. (2004) and Bousquet et al. (2008), based on approximate pressure and temperature ranges for metamorphic facies (Philpotts & Ague, 2009). Petrologically-determined pressure-temperature pathways for a range of lithologies and from various locations within the Western Alpine metamorphic belt, typically exhibit clockwise direction burial and exhumation pathways (Figure 2b). This subduction related metamorphism is, in some places, overprinted by a thermally dominated metamorphic event, e.g. Lucomagno nappe heating during decompression (Wiederkehr et al., 2008). This thermal perturbation within the central-eastern Alps is known as the Lepontine Dome, and is characterized by a metamorphic domal structure of concentric thermal isograds (e.g. Steck & Hunziker, 1994) that presumably cross-cut early-Alpine high-pressure, low-temperature nappe boundaries of the Penninic units (e.g. Burg & Gerya, 2005). This heating event reaches amphibolite to granulite facies conditions c. 600 ± 150°C (e.g. Engi et al., 1995) dated between 40–30 Ma (e.g. Schlunegger & Willett, 1999), as well as local anatexis close to the late Alpine Bergell intrusion (32.8–30 Ma: von Blackenburg, 1992; Oberli et al., 2004; Gregory et al., 2009; Gianola et al., 2014). In cross-section, late-Alpine thermal overprinting is confined to rocks derived from the European plate, reaching the highest structural levels at the Monte Rosa and Antrona contact (Figure 2c) (Bousquet et al., 2008). Compared to earlier subduction related metamorphism, the mechanisms for the late thermal event is still disputed, with interpretations based on viscous heating or increased radiogenic heat production (e.g. Jamieson et al., 1998; Burg & Gerya, 2005).

Many numerical studies have been undertaken in order to characterize the mechanisms of exhumation of HP and UHP rocks within Alpine-type collisional belts (Burov et al., 2001; Butler et al., 2014; Gerya et al., 2002; Stöckhert & Gerya, 2005; Warren et al., 2008; Yamato et al., 2007, 2008; Ruh et al., 2015). Many of these studies trace individual numerical markers (Gerya & Yuen, 2003) in order to assess P-T-time trajectories of both continental and oceanic crustal material (e.g. Butler et al., 2014; Gerya et al., 2002; Stöckhert & Gerya, 2005; Warren et al., 2008; Yamato et al., 2007, 2008; Ruh et al., 2015). As stated above, several petrological studies have made considerable efforts to compile large datasets of peak metamorphism related to subduction in the Alps (e.g. Bousquet et al., 2008). However, no numerical modelling studies, to the best of our knowledge, have attempted to reproduce, with comparable resolution, the large-scale metamorphic architecture throughout the Western Alps (Figure 2).

3 Numerical modelling approach

3.1 Model design

Model dimensions are 1600×680 km and we employ a global resolution of 1×1 km. Modelled units include a 25 km thick mechanically heterogeneous upper crust and an 8 km thick homogeneous lower crust (Figure S1b,c). The lithospheric mantle extends down to 120 km depth and we include the upper mantle down to a depth of 660 km. We apply tectonic forces by prescribing the material inflow/outflow velocities at the lateral boundaries (Figure S1a,d). In order to be applicable to the tectono-metamorphic evolution of the Western Alps, the model is divided into 4 distinct periods of activity, analogous to the Wilson Cycle involving embryonic oceans (e.g. Wilson, 1966; Dewey & Burke, 1974; Beaussier et al., 2019; Erdős et al., 2019; Chenin et al., 2019), which include: 1) Extension (50 Myr, applying 1.0 cm yr^{-1} absolute boundary velocity) of a rheologically heterogeneous lithosphere (see Table S1 and Figure S1) which leads to the formation of magma-poor continental margins bounding a marine basin floored by exhumed mantle. 2) A 60 Myr period without far-field extension or convergence (0 cm yr^{-1} applied boundary velocity) allowing for thermal equilibration of the evolved basin margin system. At the end of this period, we parameterize a serpentinization front propagating through the upper portions of the mantle exhumed in the basin. 3) Convergence is applied with 1.5 cm yr^{-1} absolute boundary velocity for 30 Myr to model subduction initiation and basin closure. 4) The applied boundary velocity is reduced to 1.0 cm yr^{-1} for the rest of the simulation during which we model subduction and exhumation of continental crustal rocks and serpentinites.

As the largest vertical movements of crustal material occurs during subduction, continental collision and exhumation, only the final stages of the model's evolution are expanded on in more detail throughout this study. Importantly, the effects the thickness of the parameterized serpentinite layer above the exhumed mantle have on the models tectono-metamorphic evolution is examined (Figure 3b–d). Two model configurations are compared that are different only in the thickness of the serpentinite layer prior to convergence (3 and 6 km). Equally, only for stages 3) and 4), the effective density for all materials are calculated beforehand, from Perple_X phase equilibria models (Connolly & Petrini, 2002), based on their corresponding pressure and temperature conditions (see Table S2).

The term "model-age (Myr)" presented in each figure, denotes the use of the numerical time being analogous to geological time used in many petrological studies, whereby the present day is regarded as 0 million years ago (Ma) and increases positively into the past. In this study, rather than regarding the beginning of the model as being 0 million years (Myr), and the end being approximately 180 Myr, we subtract each numerical time with the total numerical time in order to have a model-age that implies the final time-step is analogous to the present-day. When applying the presented models to the Western Alps, relative ages of events should be considered, not absolute ages.

Further details concerning the applied petrological–thermomechanical model are given in the supplementary material.

3.2 Defining numerical metamorphic facies

In order to assess the distribution of metamorphic facies within the modelled collisional orogen, detailed pressure-temperature-time histories for numerical markers are analyzed. A Marker-in-Cell method (Gerya & Yuen, 2003) is employed to transport physical properties throughout the numerical grid. Up to 56 Million Lagrangian markers are used to transport physical properties at each time step. From the 56 Million markers in total, *c.* 10'000 representative markers are chosen for each simulation from the continental passive margin prior to subduction (Figure 4a and d).

Following the *P-T* trajectory of markers during subduction, the maximum values of pressure and temperature are used to define a metamorphic facies (Figure 2b). This metamorphic facies identity at peak conditions is then stored for each individual marker regardless of its position during subsequent exhumation. Although a somewhat oversimplified metamorphic facies grid (Philpotts & Ague, 2009), i.e. neglecting subdivision such as upper greenschist facies and blueschist subdivisions etc., the main subdivisions are captured, e.g. eclogite–(U)HP transition defined by quartz–coesite, and a limiting geothermal gradient of 5°C/km for forbidden zone conditions is implemented (Figure 2b). These metamorphic facies divisions are similar to those used in studies characterising the metamorphic structure of metasediments throughout the European Alps (Figure 2) (e.g. Bousquet et al., 2008).

Since we are assessing subduction related metamorphism, i.e. peak metamorphic conditions, several assumptions are made. Firstly, a major assumption is that peak metamorphic conditions define an equilibrium state in a rock, and thus peak metamorphic rates are attained at peak conditions (e.g. Spear, 1989). Secondly, rocks defined by facies domains are assumed to be saturated and in equilibrium with water. Thirdly, we do not define transition zones between facies that could correspond to variations in bulk rock compositions or kinetic factors, which is somewhat a mixture of the first two assumptions (Philpotts & Ague, 2009). Overall, we do not specify mineral assemblages that characterize metamorphic facies, rather, we infer the range of *P-T* conditions that would define an assemblage. This enables us to build a picture on the relative *P-T* conditions for subducted continental lithosphere (Ghent, 2020).

A notable caveat of this numerical method is that the pressure maximum and temperature maximum of *P-T* pathways rarely correspond to the same point in *P-T* space. Therefore, we evaluate two peak metamorphic condition scenarios: 1) maximum temperature and corresponding pressure (herein referred to as max. temperature), and 2) maximum pressure and corresponding temperature (herein referred to as max. pressure). A graphical representation of this max. pressure and max. temperature and the resulting computed metamorphic facies disparity can be found in the supplementary material (Figure S2).

4 Results

Lithospheric extension leads to crustal break-up and the formation of two conjugate asymmetric magma-poor (see depth of 1300°C isotherm in Figure 3a) continental margins. At 70 Myr, a ca. 360 km wide marine basin has opened which is floored by exhumed mantle material (Figure 3b). Convection in the upper mantle has stabilised the mechanical thickness of the lithosphere to ca. 120-140 km (region without velocity glyphs in Figure 3b). During convergence, subduction initiation is horizontally-forced, favoured by thermal softening (Kiss et al., 2019, 2020) and occurs below the distal portions of the continental hyper-extended margin (Figure 3c). The location and polarity of the evolving subduction is not prescribed, but evolves spontaneously in both model configurations (3 and 6 km serpentinite layer thickness). During basin closure, the serpentinites are sheared off the subducting slab and eventually reorganise along the subduction interface (Figure 3d). For this study, we focus mainly on the model evolution after basin closure, from the onset of subsequent continental subduction during the final 40 Myr (Figure 4).

4.1 Model evolution: subduction and exhumation

We use color-coding of the markers by their initial paleogeographic position prior to subduction relative to the hyper-extended margin to study the marker trajectories during subduction, collision and exhumation (Figure 4). Furthermore, we analyse representative *P-T* pathways of individual markers (Figure 4). Numerical simulations with a 3 km serpentinite thickness (Figure 4a-c) subduct continental portions of the distal hyper-extended domain to depths of >100 km. However, these high-pressure domains are unable to exhume to depths shallower than 40 km (Figure 4c), and are prevented from reaching the surface by the over-riding plate. These domains do not retain their coherency and subsequently form a mixture below the over-riding plate (Figure 4c). The over-riding plate also forms a strong buttress to the more proximal domains towards the foreland, preventing them from being subducted (Figure 4a and c). This deformation behaviour subsequently initiates foreland-directed folding and thrusting of continental material at shallow depths, as seen by the weak and strong ellipses within the subducting continental lithosphere (Figure 4c).

Numerical simulations with a 6 km serpentinite thickness (Figure 4d-f) subduct continental portions of the distal hyper-extended domain to depths of >100 km. Exhumation of these particles to < 5 km depth is observed (Figure 4f). *P*-*T* trajectories for representative markers within the subducting crust exhibit a clockwise burial and exhumation pathway (Figure 4f). Notably, the coherency of subducted and exhumed continental portions is maintained, where the former paleogeographic transition from distal to proximal can still be observed in the final geometry, having distal parts within the core of the orogeny and proximal portions towards the foreland (Figure 4f). Exhumation of continental markers follows a near-isothermal/cooling decompression pathway back to the surface (Figure 4f).

Figure 5 shows the temporal evolution of pressure, temperature and depth for markers indicated in Figure 4 for both 3 km and 6 km serpentinite thicknesses. Due to lack of exhumation of deeply subducted particles for the 3 km serpentinite model, we do not observe notable cooling after peak conditions are attained (Figure 5a). In contrast, for the 6 km serpentinite model we observe cooling after peak conditions are attained. For both models, we observed that peak values of P and T do not occur at the same time (Figure 5a and b). Typically, peak temperature values post-date peak pressure values with larger discrepancies occurring for models with 3 km serpentinite (Figure 5a).

Exhumation velocities for 3 km serpentinite models do not on average exceed 5 mm/yr (Figure 5c). Exhumation velocities for 6 km serpentinite reach up to 15 mm/yr and hence exceed in some places subduction-related burial velocities (Figure 5d), which are approximately 7 mm/yr (for a 45 degree subduction angle and 10 mm/yr convergence velocity).

Significant deviations from lithostatic pressure are observed for particles that are not deeply subducted (red circle marker, Figure 4e, f, 5b and S2). Such deviation occurs where pressure values are *c.* 0.4 GPa higher compared to the corresponding lithostatic estimates of pressure (note similar peak P for red and purple circles in dashed box in Figure 5b, but disparities in peak depth Figure 5d).

4.2 Peak metamorphic conditions

Peak metamorphic conditions of continental markers that are subducted during convergence are presented in Figure 6. For more or less similar areas within the hyper-extended margin (Figure 4a and d), the distribution of peak P and T conditions for models with 3 km and 6 km serpentinite vary considerably (Figure 6). The paleogeographic position of markers prior to subduction also varies for the two models. For 3 km serpentinite, the range of peak *P*-*T* conditions spans a considerable range of pressures, however, the temperature ranges for the corresponding pressure values are more narrow for max. temperature values (Figure 6a), compared to max. pressure values (Figure 6b). The paleogeographic position shows trends whereby portions that only experience lower grade conditions originate from the more proximal portions of the hyper-extended margin, compared to portions that experience high grade conditions from distal regions (Figure 6a and b). For 6 km serpentinite models, the temperature ranges for the corresponding pressure values span a broader temperature range compared to 3 km models (Figure 6c and d). This temperature range does not vary as considerably between max. temperature (Figure 6c) and max. pressure (Figure 6d) compared to 3 km serpentinite models. Paleogeographic position is observed to correlate stronger with temperature rather than pressure, with more proximal regions reaching higher peak temperatures relative to more distal regions (Figure 6c and d).

Considering only the particles that are subducted and exhumed to <20 km depth (Figure 7), we can observe a large difference for models with 3 km serpentinite that do not reach >1 GPa and >400°C (Figure 7a and b), compared to 6 km serpentinite that reach >3.0 GPa and >600°C (Figure 7c and d). The majority of ages for peak pressure and temperature values of the 3 km serpentinite model are late in the models evolution (15–5 Myr before the model stops at 0 Myr) (Figure 7a and b). Peak metamorphic ages for the 6 km serpentinite model that use max. temperature show a trend of older ages (25–5 Myr) compared to 3 km serpentinite, where we can observe younger ages at higher temperatures and lower pressures (e.g. 0.5 GPa and 400°C, Figure 7a). Peak metamorphic ages corresponding to max. pressure values in 6 km serpentinite models show predominantly older ages (40–5 Myr) compared to max. temperature values (Figure 7c). Ages for max. temperature values exhibit a general trend of older ages for peak metamorphism with increasing grade (Figure 7d). Ages for max. pressure values exhibit a general trend of younger ages for peak metamorphism with increasing grade (Figure 7d).

As outlined in section 3.2, peak metamorphic facies are mapped within the simulated orogen for continental crust that has been subducted and exhumed. Figure 8a and c shows the metamorphic facies distribution for the 3 km serpentinite model based on peak P-T values corresponding to max. temperature (Figure 8a and b), and max. pressure (Figure 8c and d). Overall, metamorphic facies are distributed in a horizontally layered manner, in section, through the orogen (Figure 8a and c). The majority of subducted particles reach eclogite facies and are confined to below *c.* 40 km depth. Minor volumes of UHP facies are present in the deeper portions of the orogen where substantial mixing has occured (*c.* 40 km) (Figure 8a and b). Higher volumes of blueschist and UHP facies are present for peak conditions corresponding to max. pressure values (Figure 8c and d), than compared to max. temperature (Figure 8a and b).

Figure 8e and g shows the metamorphic facies distribution for 6 km serpentinite model. Overall, metamorphic facies of exhumed continental regions <20 km are distributed laterally across the orogen. The highest grades are observed within the core of the orogen closer to the overriding plate and decrease in grade towards the foreland (Figure 8e and g). For peak metamorphic values corresponding to max. temperature, metamorphic grades ranging from UHP, eclogite, blueschist, greenschist and zeolite are exposed within 20 km depth (Figure 8e). Similar to the 3 km serpentinite mode, the 6 km serpentinite model also contains relatively larger volumes of UHP and blueschist facies for peak conditions corresponding to max. pressure values (Figure 8g and d), compared to max. temperature (Figure 8e and f). High temperature amphibolite facies occur in small volumes between 30–40 km depth for max. temperature models (Figure 8e), something not observed in max. pressure models (Figure 8g).

5 Discussion

5.1 Applicability to the Western Alps

The variation in thickness of serpentinized exhumed mantle (3 and 6 km), separating the hyper-extended passive margins formed during rifting, has a dramatic effect on the subduction and exhumation style in the modelled collisional orogens. In our models, the initial serpentinite thickness is a parameter that controls the strength of the emerging subduction interface. The typical thickness of natural serpentinite layers formed in the Piemonte-Liguria domain was likely less than 3 to 6 km, however, such small thickness cannot be resolved numerically (McCarthy et al., 2020). Equally, in nature the developing plate interface strength may be controlled by more complex processes such as fluids, reactions, or partial melting. A result of the different subduction-exhumation styles, caused by different serpentinite thickness and hence subduction interface strength, is invariably the distribution of exhumed peak metamorphic facies (Figure 8 and 10). Peak metamorphic conditions are indicative of the depth distribution (pressure) and paleogeotherms (temperature) within a subduction zone, that are "fossilized" via subsequent exhumation to the surface. An important part in this "fossilization" process is the ability to exhume deeply buried material. The addition of a further petrological constraint by way of serpentinite thickness, as well as thermodynamically constrained densification during subduction increases the applicability of the presented petrological–thermomechanical model to natural orogens such as the Western Alps (Figure 1 and 2).

For models with a 3 km serpentinite thickness (Figure 8a and c), the overall spatial distribution of peak metamorphic facies does not agree with natural metamorphic distributions in the Western Alps (Figure 2c and d). The magnitude of peak metamorphic grades for a serpentinite thickness of 3 km is, however, in agreement with natural orogens (Figure 8b and d). However, the ultimate fate of high-pressure and ultra high-pressure domains is to reside at depths of >40 km, which is evident in the layered metamorphic architecture and testifies to an almost steady-state metamorphic environment (Figure 8a and c), as well as the inability to observe closed clockwise P-T loops (Figure 8b and d). This inability to exhume high-grade portions of subducted continental material is largely due to the overriding plate (Figures 4b, c, 8a and c). The overriding plate prevents high-pressure material from exhuming by preventing the serpentinite-rich interface between the exhuming portions and overriding plate to propagate to the surface (Figure 4b and c). This is in stark contrast to models with a 6 km serpentinite thickness (Figure 8e and d), whereby the low viscosity, serpentinite-rich interface is allowed to propagate to the surface (Figure 4e), thus allowing for and facilitating the exhumation of high-pressure domains (Figure 4f). This is evident in the metamorphic architecture of the present-day configuration, whereby we observe a high-pressure internal zone close the to subduction interface, with decreasing metamorphic grade towards the foreland (Figure 8e and g).

The resulting metamorphic architecture for a model with a parameterized 6 km serpentinite layer, at the first-order, agrees with the metamorphic distribution throughout the Western Alps (Figure 2). The metamorphic distribution even predicts the subduction polarity (Ernst, 1971, 1972), whereby the direction of increasing grade is the direction of lower-plate subduction (Figure 10). The metamorphic distribution preserves the subduction related metamorphic architecture, and serpentinite thickness dictates in part the 'fossilization' process by allowing exhumation of high-pressure domains to the surface via the 'lubrication' of a low-viscosity subduction interface. The widespread occurrences of serpentinite associated with high-pressure domains within the Western Alps, e.g. the Zermatt-Saas ophiolite (e.g. Forster et al., 2004), clearly attests to their involvement in exhumation processes (Schwartz et al., 2001; Yang et al., 2020; Agard et al., 2018; Ruh et al., 2015; Guillot et al., 2015; Chang et al., 2009).

Similar to the importance of the parameterized serpentinite layer above the exhumed mantle, the role of the inherited hyper-extended margin structure and rheology (Figure 1a) prior to convergence is likely an important contributor defining the ultimate metamorphic architecture (Figure 3 and 10). For the presented models, a period of lithospheric extension has resulted in two passive margins (Figure 3b), in reality, however, the structure of these passive margins is not as simple. A more heterogeneous passive margin, with more continental 'boudins' (Figure 1a), may result in different areas of strain localization during convergence. These continental boudins would be analogous, in the western Alpine Tethys, to the Inner-Penninic regions of European origin, and the Sesia-Dent Blanche regions of the distal Austro-Alpine margin (Figure 1a) (Dal Piaz et al., 2001).

Inherited structural complexity deriving from extensional tectonics within the former passive margin (Figure 1a) may also contribute to the structurally complex and minor volumes of exhumed coherent (U)HP units observed throughout the Western Alps, e.g. Brossasco-Isasca unit (BIU) within the Dora Maira massif (Figure 2) (e.g. Rubatto & Hermann, 2001; Groppo et al., 2019). In our models of 6 km serpentinite we have subducted and exhumed particles which have P-T values similar to that of most units of the Dora Maira massif (2–2.4 GPa and 500–540 C: Groppo et al., 2019). However, the ultrahigh-P and high-T particles of the BIU are not exhumed (Figure 10d). The BIU is very small (c. 1 km thickness), and our model cannot resolve shear zones around such thin units due to the numerical resolution of 1 km^2. That being said, the markers unable to exhume indicate a model subduction geotherm with a reasonable P-T trend, and in nature the BIU unit might be exhumed as individual slice, but the mechanism is not clear at the present moment and may become more apparent with increasing numerical resolution. Simple numerical models have already shown that significant strain localization around the BIU might have enabled exhumation of the BIU as an individual slice along the subduction interface after its detachment from the subducting European plate (Schmalholz & Schenker, 2016).

5.2 Predictive modelling of metamorphic facies

Using the peak pressure and temperature incurred by numerical particles during their subduction and exhumation clockwise trajectory, is a good approximation for the distribution of subduction-related metamorphic facies (Figure 8). It is a somewhat oversimplification to use peak values of P and T to assess the distribution of metamorphic facies. However, the assumptions made here with regards to "freezing" in time the peak metamorphic grades expressed in petrology as assemblages (section 3.2), do not differ considerably from the assumptions made when applying geo-thermobarometers to natural samples. Namely, 1) the assumption of equilibrium in pseudo-section calculations, 2) equilibrium with water or water saturated conditions, 3) textural identification of peak metamorphic conditions, and 4) the neglection of kinetic factors.

Questions arising from the assumption that the relative phases in a peak assemblage equilibrated at a single P-T condition are not evaluated in this study (e.g. Spear, 1989; Spear et al., 2017). However, it is worth labouring the point that this assumption predicts well the large-scale metamorphic architecture in our numerical model. Such factors as the kinetics of metamorphic reactions during prograde pathways focus on the mineral scale, whereas peak metamorphic conditions applied to the entire orogeny focus on regional-scale trends (Figure 2). Considerable effort has been made to map out the larger-scale subduction related metamorphism throughout the Western Alps (e.g. Agard et al., 2002; Babist et al., 2006; Beltrando, Compagnoni, & Lombardo, 2010; Oberhänsli et al., 2004; Bousquet et al., 2008), and this accumulation of data primarily focuses on peak P and T conditions.

Minor disparities arises within the metamorphic architecture of the modelled orogeny when using max. P or max. T values that define a facies in P-T space (Figure 8 and S2). Although the larger-scale metamorphic structure is consistent, occurrences of blueschist facies and UHP facies P-T conditions are more widespread in both 3 km and 6 km serpentinite models (Figure 8c and g). This is primarily due to peak P and T values not being consistent (Figure S2), e.g. where a decrease in P occurs during continued heating. Peak T can reach between 50–100°C hotter than the corresponding T at peak P. This decrease in P may be due to decompression after periods of tectonic pressure (red circle marker, Figure 4e, f and Figure 5b), or due to continued heating during decompression which is suggested in some areas of the Western Alps (e.g. Wiederkehr et al., 2008; Bousquet et al., 2008; Rubatto & Hermann, 2001). The observed increase in blueschist and UHP facies occurrences for maximum P values likely reflects the pressure dependent slope of the lower boundaries of metamorphic facies in P-T space (Figure 2a). This

P dependency is exemplified if we look at what facies are being replaced by blueschist and UHP facies when considering max. P. Typically, blueschist facies replace greenschist facies, and UHP facies replace HP facies (Figure 8e and g). Again it is important here to stress the use of metamorphic facies in representing relative P-T conditions (Ghent, 2020).

Observations of blueschist facies occurrences throughout orogenic zones are predominantly confined to the Phanerozoic, e.g. the European Alps and Franciscan Complex (Ernst, 1972; Ghent, 2020; Palin et al., 2020). Amongst several interpretations for the lack of blueschist facies metamorphism older than 250 million years, a higher geothermal gradient in the past has been proposed (e.g. Thompson, 1984; Brown, 2014). A higher paleo-geotherm in the past may have resulted in weakening of subducted rocks due to temperature dependent rheologies, therefore lowering the effective strength of rocks and their propensity to facilitate deviations from lithostatic P, and even inhibiting subduction altogether (e.g. Faccenda et al., 2008; Poh et al., 2020). In reality, a mixture of max. P and max. T for defining modelled metamorphic facies may be more realistic for younger orogens.

5.3 Syn-convergent exhumation

As outlined in section 5.1, the presence of serpentinite allows for the lubrication of a low viscosity interface between the overriding plate and the exhuming continental material. This boundary is typically called a subduction, or plate interface and exhumed portions of this structure can be observed throughout the Western Alps, e.g. at the base of the Adria-derived Dent Blanche unit (Angiboust et al., 2014).

Progressive exhumation of high-pressure footwall material along a major normal sense shear zone has been suggested for several regions throughout the Alps (Beltrando, Lister, et al., 2010; Bucher et al., 2003; Campani, Herman, & Mancktelow, 2010; Campani, Mancktelow, et al., 2010; Cawood & Platt, 2020; S. Reddy et al., 1999; S. M. Reddy et al., 2003; Wheeler et al., 2001; Ring & Merle, 1992; Mancktelow, 1985; Manzotti, Zucali, et al., 2014). Although shear indicators are well documented, the actual mechanism for generating such structural features is still unclear (e.g. Bucher et al., 2003). Two scenarios may be at play: 1) periods of intermittent far-field extension, that is plate divergence, between periods of convergence (e.g. Beltrando, Lister, et al., 2010; S. Reddy et al., 1999), or 2) extrusion of subducted material during continuous plate convergence (e.g. Chemenda et al., 1995; Duretz et al., 2012; Froitzheim et al., 2003, 2006; Keller et al., 2005; Butler et al., 2014).

Figure 9 demonstrates the shear sense indicators relevant across the subduction zone interface in the presented 6 km serpentinite model. An initial rectangular box who's long axis is parallel with the major subduction zone interface between the overriding plate and exhuming continental material has been plotted using advected numerical markers (Figure 9a). During continued subduction, the box is progressively sheared with a normal sense of shear as the material is being exhumed (Figure 9b-d). The sides of the initial rectangle parallel to the subduction zone interface remain at fixed distances from one another during progressive exhumation, attesting to the coherency of the exhuming material (Figure 9c and d). Whereas, the sides of the initial rectangle perpendicular to the subduction zone interface are significantly extended (Figure 9d). Using these shear indicators we can observe local normal sense (extensional) shear between the overriding plate at the top of the exhuming continental units, during overall convergence. These observations agree with shear indicators resulting from extrusion of subducted material (e.g. Chemenda et al., 1995; Duretz et al., 2012; Froitzheim et al., 2003, 2006; Keller et al., 2005), rather than intermittent far-field extensional tectonics, due to plate divergence, during orogenesis. Extrusion of subducted material also allows for the local extension and subsequent separation of upper plate material (Figure 9c and d, yellow particles).

Similarly, such separation of the Adriatic upper plate could have occurred, and could explain the far-travelled Adria-derived units within the external domains of the Western Alps, such as the Gets and Simme nappes, which have been correlated to the Adriatic passive margin (Figure 1) (Escher et al., 1997; Gasinski et al., 1997; Ferrando et al., 2004).

Advanced numerical modelling studies of synconvergent exhumation applied to the Western Alps, such as Butler et al. (2014), also show that plate divergence is not necessary to explain local extensional tectonics associated with (U)HP exhumation. Exhumation within such models, e.g. Inner Penninic domains of the Western Alps, typically occurs as composite stacked plumes with significant tectonic mixing and requires significant erosion. The modelled P-T-time trajectories coincide with petrological studies, but the larger-scale metamorphic architecture is not investigated (Butler et al., 2014). In our study, progressive exhumation of HP and (U)HP rocks along a major normal sense shear zone at the plate interface maintains coherency. This coherency is observed in the present-day configuration (Figure 10), whereby the metamorphic architecture preserves equilibration at pressure and temperature conditions within the deeply-seated subduction environment (Figure 10d). Furthermore, due to the local extension of the upper plate, our model does not require significant erosion to enable significant exhumation.

6 Conclusions

The applied petrological–thermomechanical numerical model for subduction, exhumation and collision during plate convergence can predict the metamorphic facies evolution and distribution during orogeny with approximately 10'000 markers recording peak temperature and pressure. The plate interface strength, which evolves during subduction, has a first order impact on the exhumation of buried rocks and hence on the subduction related metamorphic facies distribution. In the model, the plate interface strength is controlled by the initial thickness of a serpentinite layer, which is either 3 or 6 km thick. A stronger plate interface, 3 km serpentinite, generates a horizontally layered metamorphic facies distribution. A weaker plate interface, 6 km serpentinite, generates a vertically layered metamorphic facies distribution, with highest grades in the core of the orogen and decreasing grades towards the foreland region. Such a metamorphic facies distribution, predicted by models with 6 km serpentinite, agrees with the first order mapped subduction related metamorphic facies distribution of the Western Alps.

Tracing thousands of numerical markers allows for the analysis of the paleogeography and age of peak metamorphism of subducted units. The paleogeographic position of subducted and exhumed portions for the model of 6 km serpentinite typically derive from the more distal portions of the subducted continental hyper-extended margin prior to subduction. This agrees with paleogeographic reconstructions for the Western Alps whereby high-grade units such as the Inner Penninic Monte Rosa, Gran Paradiso and Dora Maira massifs derive from distal regions of the European margin. The age distribution of peak metamorphism for the model of 6 km serpentinite shows a weak overall trend whereby higher grades of peak metamorphism occur during earlier periods of the model history.

The modelled metamorphic architecture is based on the simple assumption that peak values of pressure and temperature reflect subduction related metamorphism during burial and exhumation of continental derived rocks. This assumption predicts well the large-scale subduction-related metamorphic structure in the Western Alps, however, differences arise when using peak pressure (*c.* 0.4 GPa tectonic pressure) or temperature (*c.* 50°C continued heating during decompression) when defining a metamorphic facies in P-T space. Metamorphic facies defined by peak temperature values closely resemble the first-order metamorphic architecture in the Western Alps, whereas peak pressure values over-estimate blueschist and UHP volumes. In nature, peak metamorphism may be

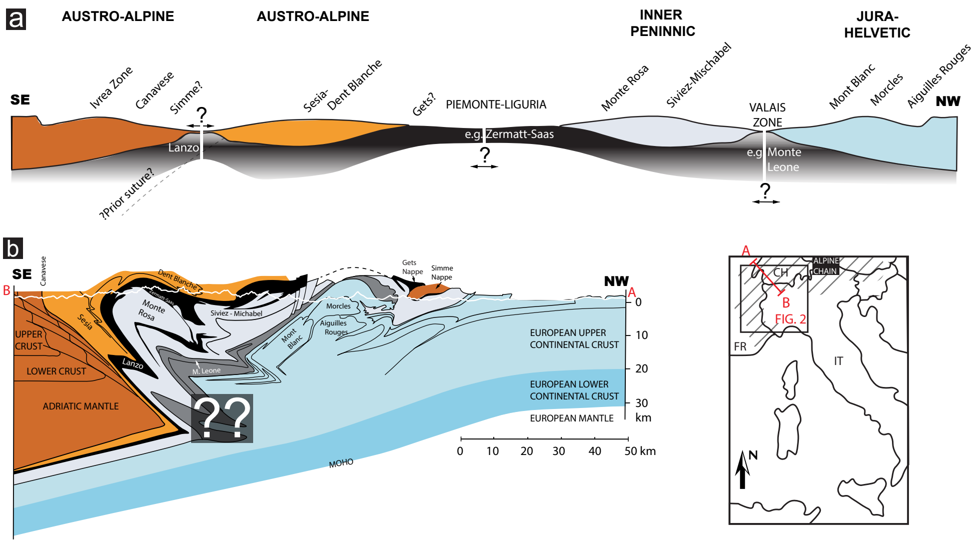

Figure 1. (a) Paleogeographic cross-section reconstruction of the western Alpine Tethys domain between the Adriatic and European margin prior to convergence (distorted horizontal and vertical scales), modified after Dal Piaz et al. (2001) and McCarthy et al. (2020). (b) Present-day cross-section of the Western Alps coloured with respect to paleogeographic domains in (a), modified after Escher et al. (1993), Escher et al. (1993) and Steck et al. (2015).

defined in some areas by a mixture of both peak temperature and peak pressure values, especially for colder geothermal gradients during more recent geological periods.

The presented numerical model predicts syn-convergent exhumation by extrusion, which is associated with the formation of large-scale normal-sense shear zones at the subduction, or plate, interface. Therefore, exhumation of (U)HP rocks can be related to local extensional kinematics and does not necessarily indicate regional-scale plate divergence.

Acknowledgments

This work was supported by the Swiss National Science Foundation grant No. 200021-165756 and 200020-163169. J.V-H thanks Lukas Baumgartner, Evangelos Moulas and Philip Groß for helpful discussions. S.M.S thanks Jean-Luc Epard for many enlightning discussions on Alpine tectonics. We would like to dedicate this study to Albrecht Steck. Data Availability Statement: Data archiving is underway.

References

Agard, P., Monié, P., Jolivet, L., & Goffé, B. (2002). Exhumation of the schistes lustrés complex: in situ laser probe 40ar/39ar constraints and implications for the western alps. *Journal of metamorphic Geology*, *20*(6), 599-618.

Agard, P., Plunder, A., Angiboust, S., Bonnet, G., & Ruh, J. (2018). The subduction plate interface: rock record and mechanical coupling (from long to short timescales). *Lithos*, *320*, 537-566.

Angiboust, S., Agard, P., Jolivet, L., & Beyssac, O. (2009). The zermatt-saas ophiolite: the largest (60-km wide) and deepest (c. 70–80 km) continuous slice of

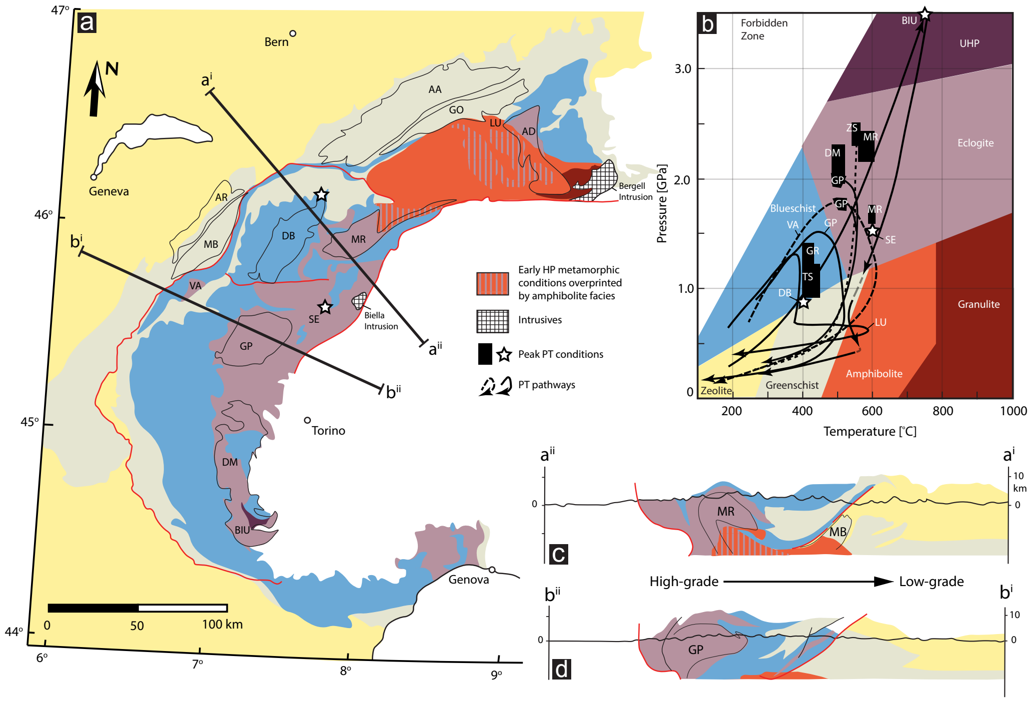

Figure 2. (a) Peak Alpine metamorphic facies distribution throughout the Western Alps with major units indicated, modified after Oberhänsli et al. (2004) and Bousquet et al. (2008) (AA = Aar massif, GO = Gotthard massif, LU = Lucomagno, AD = Adula, MR = Monte Rosa, DB = Dent Blanche, GP = Gran Paradiso, DM = Dora Maira, BIU = Brossasco-Isasca unit, SE = Sesia, VA = Valaisan, MB = Mont Blanc massif, AR = Aiguilles Rouge massif). (b) Approximate pressure-temperature metamorphic facies grid (modified after Philpotts & Ague, 2009) with representative P-T estimates for Western Alpine units (dashed and solid lines are used for clearer visualization), BIU = (Rubatto & Hermann, 2001), MR = (Luisier et al., 2019; Vaughan-Hammon et al., 2021), SE = (Lardeaux & JM, 1982; Vuichard & Ballevre, 1988), VA = (Goffé & Bousquet, 1997; Bousquet et al., 2002; Wiederkehr et al., 2007), GP = (Bousquet et al., 2008; Manzotti et al., 2018), LU = (Wiederkehr et al., 2008), DB = (Cortiana et al., 1998), DM = (Liati et al., 2009), TS = Tambo Suretta (Challandes et al., 2003), ZS = Zermatt-Saas (Angiboust et al., 2009), GR = Grisons (Bousquet et al., 2002). (c) and (d) cross-sections of peak metamorphic facies with direction of decreasing subduction related metamorphism indicated.

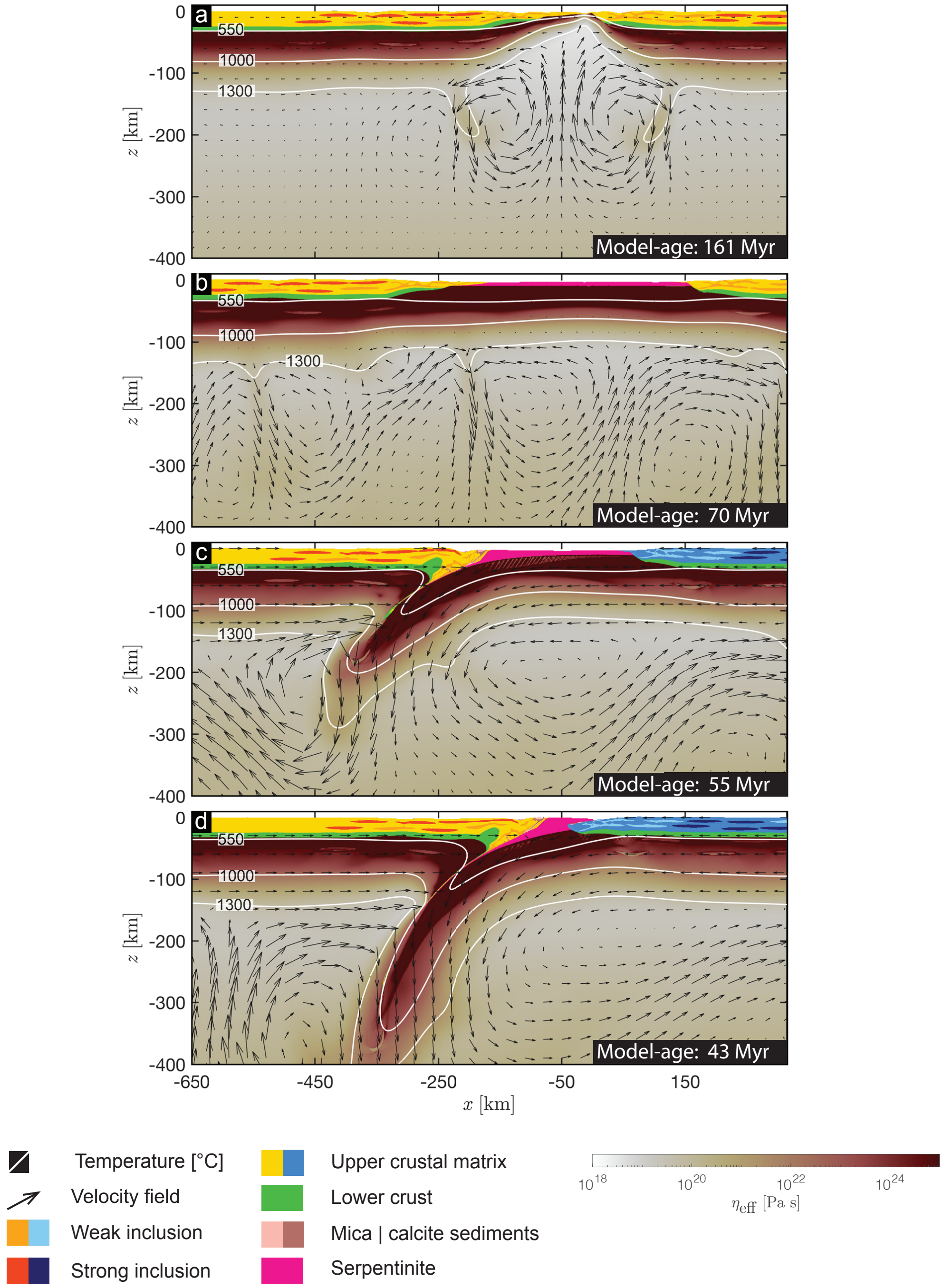

Figure 3. Numerical model evolution of phases and effective viscosity (η_{eff}) of the mantle prior to continental convergence. (a) Rifting of continental lithosphere and exposure of sub-lithospheric mantle. (b) Thermal relaxation of model and serpentinization of upper portions of exposed mantle. (c) Convergence of model and single-sided subduction initiated below distal portions of the hyper-extended continental margin. Continental phase colours changed to blue for subducted crust in order to delimit and imitate the European margin subducting below Adria (Figure 1). (d) Onset of continental collision and subduction of continental crust.

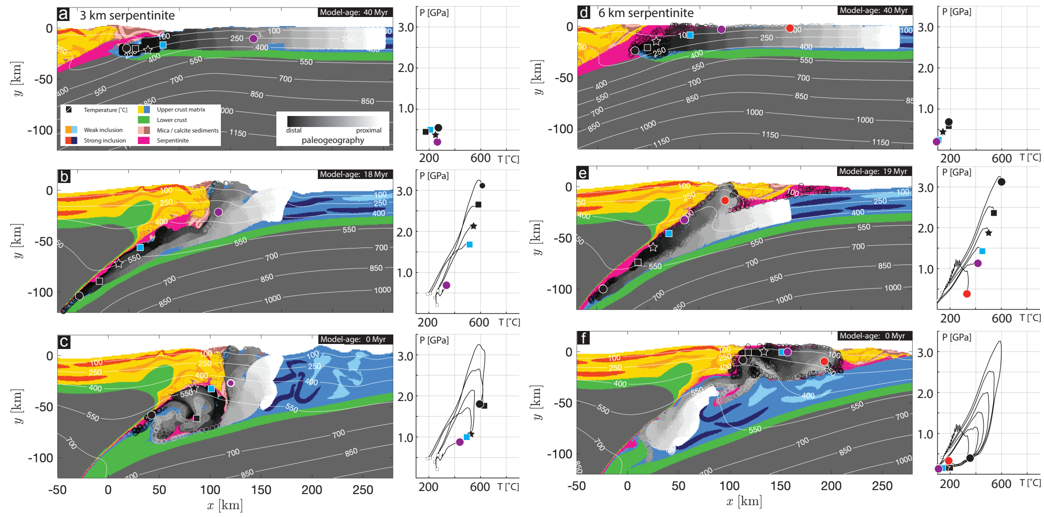

Figure 4. Model phase evolution of subduction and exhumation of continental crust. (a)-(c) 3 km serpentinite numerical model where markers are coloured by paleogeographic position at the former hyper-extended margin, as well as representative P-T evolution for subducted continental particles. (d)-(f) 6 km serpentinite numerical model where markers are coloured by paleogeographic position at the former hyper-extended margin, as well as representative P-T evolution for subducted continental particles.

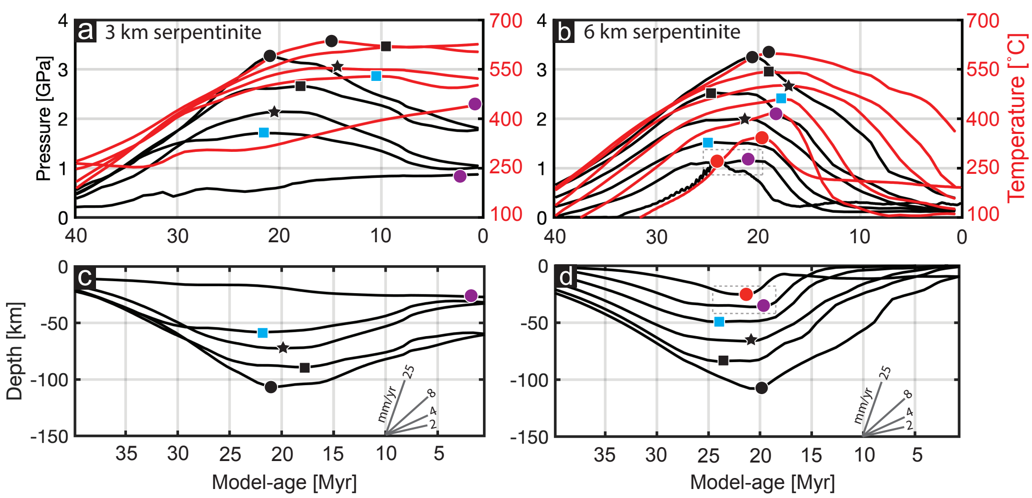

Figure 5. Marker evolution of continental particles during subduction, where symbols indicate the conditions of peak metamorphic grade (same as those in Figure 4). (a) and (b) P-T-time evolution with peak temperature and peak pressure conditions indicated. (c) and (d) depth-time evolution with maximum depth indicated and representative exhumation velocity gradients. Dashed boxes in (b) and (d) highlight the contribution of tectonic pressure for the red circle marker.

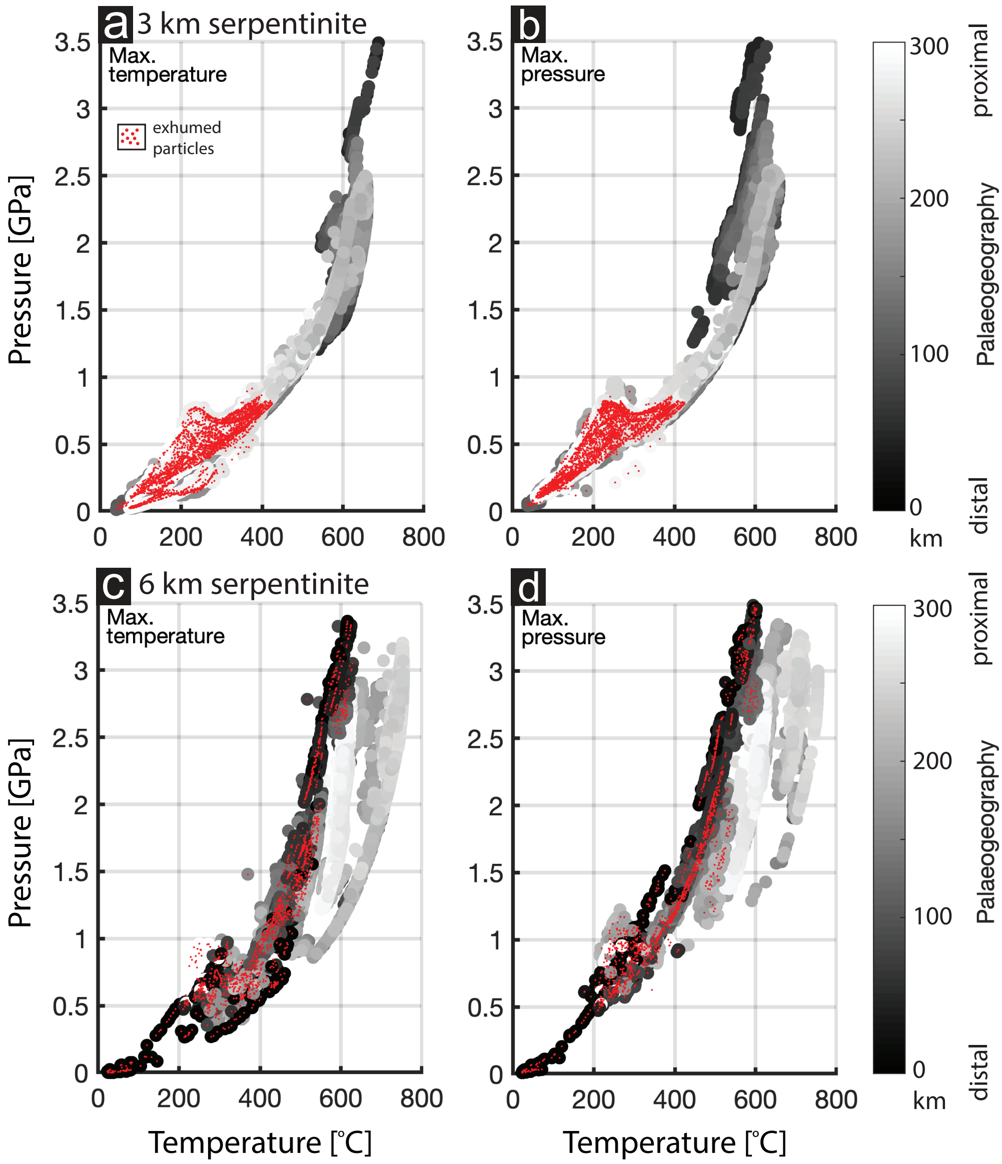

Figure 6. Maximum *P-T* conditions attained by subducted particles (indicated in Figure 4), coloured as a function of initial paleogeography within the hyper-extended margin prior to subduction, particles exhumed to <20 km depth are indicated in red. Max. temperature corresponds to *P-T* conditions taken using the maximum temperature attained during subduction. Max. pressure corresponds to *P-T* conditions taken using the maximum pressure attained during subduction (see methods section 3.2).

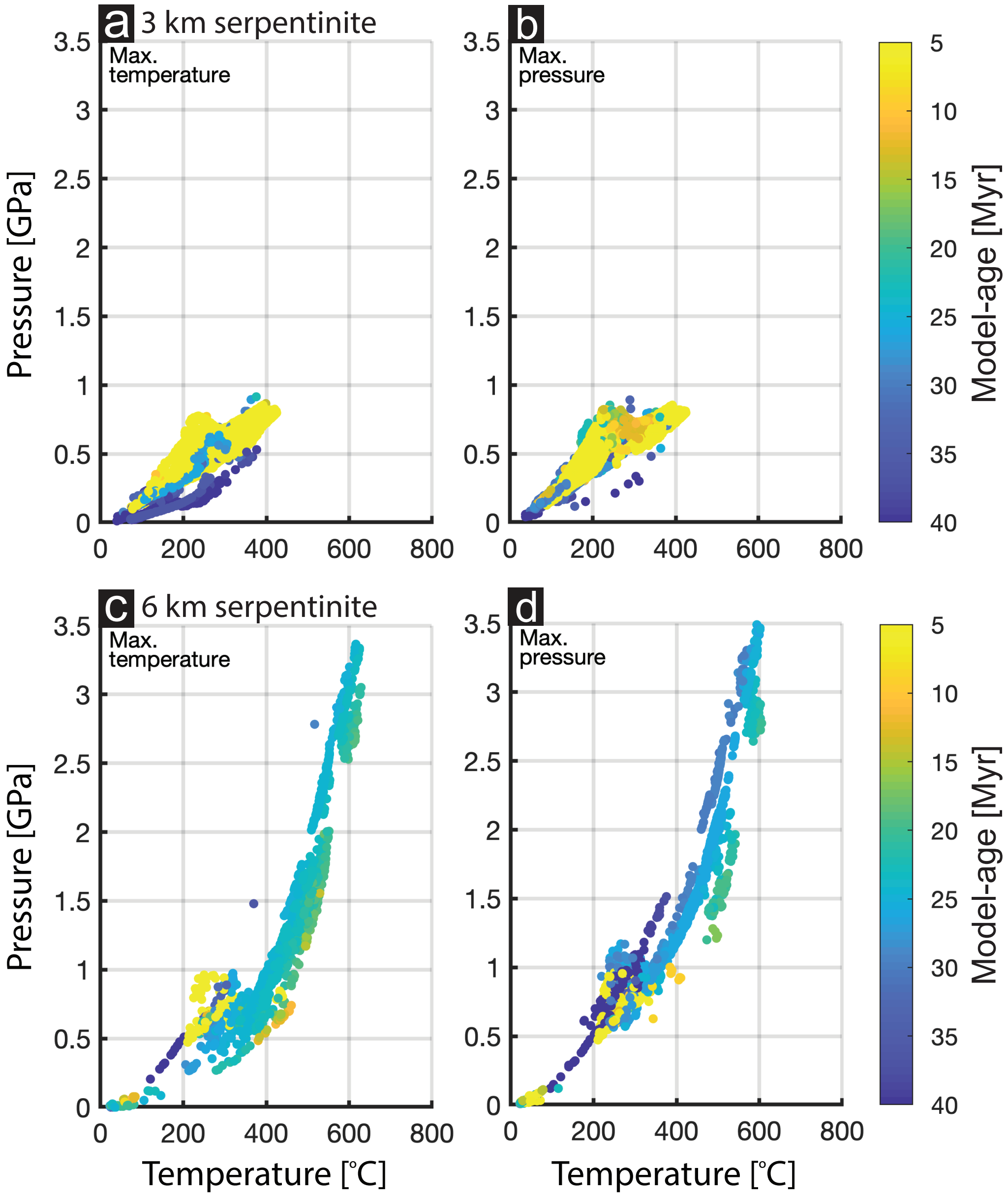

Figure 7. Maximum P-T conditions attained by particles subducted and exhumed to <20 km depth, coloured as a function of age of peak metamorphic conditions. Max. temperature corresponds to P-T conditions taken using the maximum temperature attained during subduction. Max. pressure corresponds to P-T conditions taken using the maximum pressure attained during subduction (see methods section 3.2).

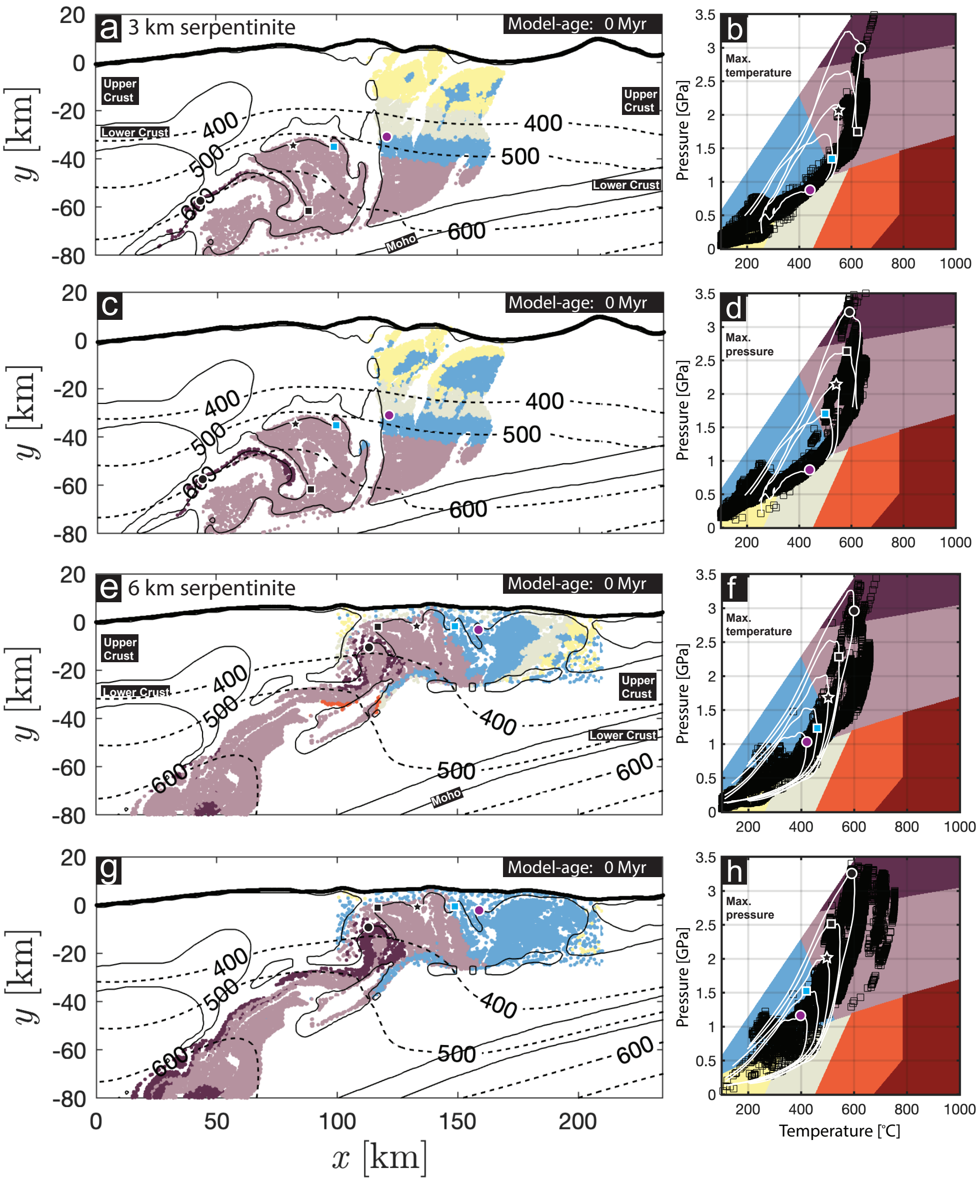

Figure 8. (a) Metamorphic facies distribution of 3 km serpentinite model based on max. temperature. (b) Representative maximum P-T conditions over metamorphic facies grid (black squares, modified after Philpotts & Ague, 2009) and representative P-T loops (similar to markers in Figures 4 and 5 where peak conditions are indicated by coloured markers). (c) Metamorphic facies distribution of 3 km serpentinite model based on max. pressure. (d) Representative maximum P-T conditions over metamorphic facies grid (black squares) and representative P-T loops (similar to markers in Figures 4 and 5 where peak conditions are indicated by coloured markers). (e) Metamorphic facies distribution of 6 km serpentinite model based on max. temperature. (f) Representative maximum P-T conditions over metamorphic facies grid (black squares) and representative P-T loops (similar to markers in Figures 4 and 5 where peak conditions are indicated by coloured markers). (g) Metamorphic facies distribution of 6 km serpentinite model based on max. pressure. (h) Representative maximum P-T conditions over metamorphic facies grid (black squares) and representative P-T loops (similar to markers in Figures 4 and 5 where peak conditions are indicated by coloured markers).

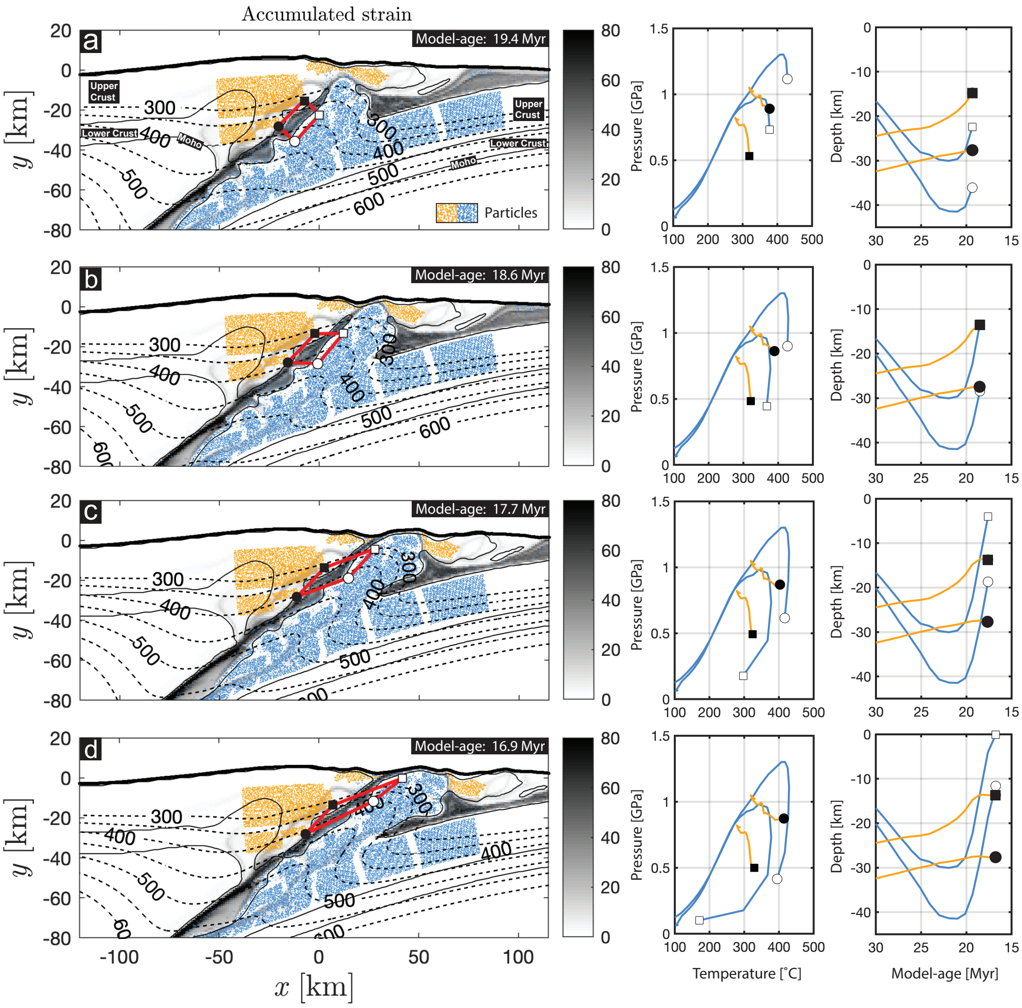

Figure 9. 6 km serpentinite model accumulated strain evolution. Particles indicated from overriding plate (yellow) and subducting plate (blue). Red box whose longest sides correspond to the upper plate and exhuming lower plate, indicating syn-convergent extensional shear during exhumation of subducted continental material across the major subduction zone interface. Corresponding *P*-*T* and Depth-time evolution plots for particles at the corners of the initial red box.

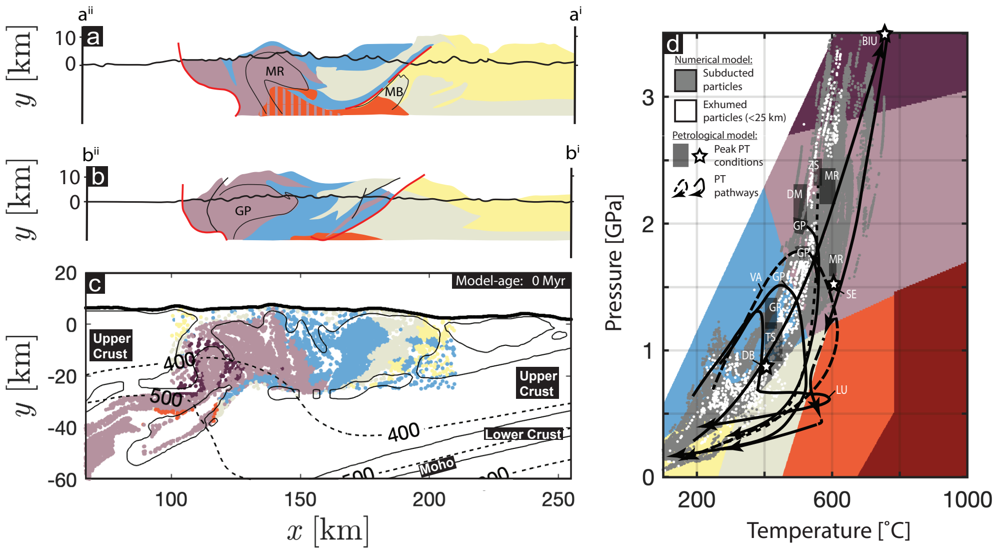

Figure 10. Comparison of petrological metamorphic facies section with numerical results. (a) and (b) petrologically-inspired metamorphic facies cross-section of the Western Alps (modified after Oberhänsli et al. (2004) and Bousquet et al. (2008)). (c) numerical results of metamorphic facies distribution for 6 km serpentinite based on maximum temperature. (d) *P-T* metamorphic facies grid (modified after Philpotts & Ague, 2009) comparing peak numerical *P-T* values (for all particles and exhumed particles) with representative *P-T* estimates for Western Alpine units (references within Figure 2).

oceanic lithosphere detached from a subduction zone? *Terra Nova*, *21*(3), 171-180.

Angiboust, S., Glodny, J., Oncken, O., & Chopin, C. (2014). In search of transient subduction interfaces in the dent blanche–sesia tectonic system (w. alps). *Lithos*, *205*, 298-321.

Babist, J., Handy, M., Konrad-Schmolke, M., & Hammerschmidt, K. (2006). Precollisional, multistage exhumation of subducted continental crust: The sesia zone, western alps. *Tectonics*, *25*(6).

Barnicoat, A., Rex, D., Guise, P., & Cliff, R. (1995). The timing of and nature of greenschist facies deformation and metamorphism in the upper pennine alps. *Tectonics*, *14*(2), 279-293.

Barrow, G. (1893). On an intrusion of muscovite-biotite gneiss in the south-eastern highlands of scotland, and its accompanying metamorphism. *Quarterly Journal of the Geological Society*, *49*(1-4).

Beaussier, S. J., Gerya, T. V., & Burg, J.-P. (2019). 3d numerical modelling of the wilson cycle: structural inheritance of alternating subduction polarity. *Geological Society, London, Special Publications*, *470*(1), 439-461.

Beltrando, M., Compagnoni, R., & Lombardo, B. (2010). (ultra-) high-pressure metamorphism and orogenesis: an alpine perspective. *Gondwana Research*, *18*(1), 147-166.

Beltrando, M., Lister, G. S., Rosenbaum, G., Richards, S., & Forster, M. A. (2010). Recognizing episodic lithospheric thinning along a convergent plate margin: The example of the early oligocene alps. *Earth-Science Reviews*, *103*(3-4), 81-98.

Berger, A., Schmid, S. M., Engi, M., Bousquet, R., & Wiederkehr, M. (2011).

Mechanisms of mass and heat transport during barrovian metamorphism: A discussion based on field evidence from the central alps (switzerland/northern italy). *Tectonics*, *30*(1).

Bousquet, R., Goffé, B., Vidal, O., Oberhänsli, R., & Patriat, M. (2002). The tectono-metamorphic history of the valaisan domain from the western to the central alps: New constraints on the evolution of the alps. *Geological Society of America Bulletin*, *114*(2), 207-225.

Bousquet, R., Oberhänsli, R., Goffé, B., Wiederkehr, M., Koller, F., Schmid, S. M., ... Martinotti, G. (2008). Metamorphism of metasediments at the scale of an orogen: a key to the tertiary geodynamic evolution of the alps. *Geological Society, London, Special Publications*, *298*(1), 393-411.

Brown, M. (2014). The contribution of metamorphic petrology to understanding lithosphere evolution and geodynamics. *Geoscience Frontiers*, *5*(4), 553–569.

Bucher, S., Schmid, S. M., Bousquet, R., & Fügenschuh, B. (2003). Late-stage deformation in a collisional orogen (western alps): nappe refolding, back-thrusting or normal faulting? *Terra Nova*, *15*(2), 109-117.

Burg, J., & Gerya, T. (2005). The role of viscous heating in barrovian metamorphism of collisional orogens: thermomechanical models and application to the lepontine dome in the central alps. *Journal of Metamorphic Geology*, *23*(2), 75-95.

Burov, E., Jolivet, L., Le Pourhiet, L., & Poliakov, A. (2001). A thermomechanical model of exhumation of high pressure (hp) and ultra-high pressure (uhp) metamorphic rocks in alpine-type collision belts. *Tectonophysics*, *342*(1-2), 113-136.

Butler, J. P., Beaumont, C., & Jamieson, R. A. (2014). The alps 2: Controls on crustal subduction and (ultra) high-pressure rock exhumation in alpine-type orogens. *Journal of Geophysical Research: Solid Earth*, *119*(7), 5987-6022.

Campani, M., Herman, F., & Mancktelow, N. (2010). Two-and three-dimensional thermal modeling of a low-angle detachment: Exhumation history of the simplon fault zone, central alps. *Journal of Geophysical Research: Solid Earth*, *115*(B10).

Campani, M., Mancktelow, N., Seward, D., Rolland, Y., Müller, W., & Guerra, I. (2010). Geochronological evidence for continuous exhumation through the ductile-brittle transition along a crustal-scale low-angle normal fault: Simplon fault zone, central alps. *Tectonics*, *29*(3).

Cawood, T. K., & Platt, J. P. (2020). Variations in the ptt of deformation in a crustal-scale shear zone in metagranite. *Earth and Space Science Open Archive ESSOAr*.

Challandes, N., Marquer, D., & Villa, I. M. (2003). Dating the evolution of c–s microstructures: a combined 40ar/39ar step-heating and uv laserprobe analysis of the alpine roffna shear zone. *Chemical Geology*, *197*(1-4), 3-19.

Chang, C.-P., Angelier, J., & Huang, C.-Y. (2009). Evolution of subductions indicated by mélanges in taiwan. In *Subduction zone geodynamics* (p. 207-225). Springer.

Chemenda, A. I., Mattauer, M., Malavieille, J., & Bokun, A. N. (1995). A mechanism for syn-collisional rock exhumation and associated normal faulting: Results from physical modelling. *Earth and Planetary Science Letters*, *132*(1-4), 225-232.

Chenin, P., Picazo, S., Jammes, S., Manatschal, G., Müntener, O., & Karner, G. (2019). Potential role of lithospheric mantle composition in the wilson cycle: a north atlantic perspective. *Geological Society, London, Special Publications*, *470*(1), 157–172.

Chopin, C. (1984). Coesite and pure pyrope in high-grade blueschists of the western alps: a first record and some consequences. *Contributions to Mineralogy and Petrology*, *86*(2), 107-118.

Chopin, C. (1987). Very-high-pressure metamorphism in the western alps: implications for subduction of continental crust. *Philosophical Transactions of the Royal Society of London. Series A, Mathematical and Physical Sciences*, *321*(1557), 183-197.

Connolly, J., & Petrini, K. (2002). An automated strategy for calculation of phase diagram sections and retrieval of rock properties as a function of physical conditions. *Journal of Metamorphic Geology*, *20*(7), 697-708.

Cortiana, G., Dal Piaz, G., Del Moro, A., Hunziker, J., & Martin, S. (1998). 40ar-39ar and rb-sr dating of the pillonet klippe and sesia-lanzo basal slice in the ayas valley and evolution of the austroalpine-piedmont nappe stack. *Memorie di Scienze Geologiche*, *50*, 177-194.

Dal Piaz, G., Cortiana, G., Del Moro, A., Martin, S., Pennacchioni, G., & Tartarotti, P. (2001). Tertiary age and paleostructural inferences of the eclogitic imprint in the austroalpine outliers and zermatt–saas ophiolite, western alps. *International Journal of Earth Sciences*, *90*(3), 668-684.

De Graciansky, P.-C., Roberts, D. G., & Tricart, P. (2011). The birth of the western and central alps: Subduction, obduction, collision. In *Developments in earth surface processes* (Vol. 14, p. 289-315). Elsevier.

Dewey, J. F., & Burke, K. (1974). Hot spots and continental break-up: implications for collisional orogeny. *Geology*, *2*(2), 57-60.

Di Vincenzo, G., Tonarini, S., Lombardo, B., Castelli, D., & Ottolini, L. (2006). Comparison of 40ar–39ar and rb–sr data on phengites from the uhp brossasco–isasca unit (dora maira massif, italy): implications for dating white mica. *Journal of Petrology*, *47*(7), 1439-1465.

Duchêne, S., Blichert-Toft, J., Luais, B., Télouk, P., Lardeaux, J.-M., & Albarede, F. (1997). The lu–hf dating of garnets and the ages of the alpine high-pressure metamorphism. *Nature*, *387*(6633), 586-589.

Duretz, T., Gerya, T., Kaus, B., & Andersen, T. (2012). Thermomechanical modeling of slab eduction. *Journal of Geophysical Research: Solid Earth*, *117*(B8).

Engi, M., Regis, D., Darling, J., Rubatto, D., Cenki Tok, B., Zucali, M., & Compagnoni, R. (2011). Dynamics in the sesia hp terrane: Combined petrochronological and structural analysis. In *Nature of the plate interface in subduction zones.*

Engi, M., Todd, C., & Schmatz, D. (1995). Tertiary metamorphic conditions in the eastern lepontine alps. *Schweizerische Mineralogische und Petrographische Mitteilungen*, *75*(3), 347-369.

Erdős, Z., Huismans, R. S., & Beek, P. v. d. (2019). Control of increased sedimentation on orogenic fold-and-thrust belt structure–insights into the evolution of the western alps. *Solid Earth*, *10*(2), 391-404.

Ernst, W. (1971). Metamorphic zonations on presumably subducted lithospheric plates from japan, california and the alps. *Contributions to Mineralogy and Petrology*, *34*(1), 43-59.

Ernst, W. (1972). Occurrence and mineralogic evolution of blueschist belts with time. *American Journal of Science*, *272*(7), 657-668.

Escher, A., & Beaumont, C. (1997). Formation, burial and exhumation of basement nappes at crustal scale: a geometric model based on the western swiss-italian alps. *Journal of Structural Geology*, *19*(7), 955-974.

Escher, A., Hunziker, J., Marthaler, M., Masson, H., Sartori, M., & Steck, A. (1997). Geological framework and structural evolution of the western swiss-italian alps. *Deep Structure of the Swiss Alps: Results of the National Research Program 20 (NRP 20)*, 205-222.

Escher, A., Masson, H., & Steck, A. (1993). Nappe geometry in the western swiss alps. *Journal of structural Geology*, *15*(3-5), 501-509.

Eskola, P. (1915). On the relations between the chemical and mineralogical composition in the metamorphic rocks of orijarvi region. *Bull. comm. géol. Finlande*,

44.
Faccenda, M., Gerya, T. V., & Chakraborty, S. (2008). Styles of post-subduction collisional orogeny: influence of convergence velocity, crustal rheology and radiogenic heat production. *Lithos*, *103*(1-2), 257–287.
Ferrando, S., Bernoulli, D., & Compagnoni, R. (2004). The canavese zone (internal western alps): a distal margin of adria. *Schweizerische Mineralogische und Petrographische Mitteilungen*, *84*(1-20).
Forster, M., Lister, G., Compagnoni, R., Giles, D., Hills, Q., Betts, P., ... Tamagno, E. (2004). Mapping of oceanic crust with" hp" to" uhp" metamorphism: The lago di cignana unit,(western alps). In *Mapping geology in italy.* Geological Society of London.
Frey, M., Desmons, J., & Neubauer, F. (1999). Metamorphic maps of the alps. an enclosure to. *Schweiz. Mineral. Petrogr. Mitt*, *79*(1).
Froitzheim, N., Pleuger, J., & Nagel, T. J. (2006). Extraction faults. *Journal of Structural Geology*, *28*(8), 1388-1395.
Froitzheim, N., Pleuger, J., Roller, S., & Nagel, T. (2003). Exhumation of high-and ultrahigh-pressure metamorphic rocks by slab extraction. *Geology*, *31*(10), 925-928.
Gasinski, A., Slaczka, A., & Winkler, W. (1997). Tectono-sedimentary evolution of the upper prealpine nappe (switzerland and france): nappe formation by late cretaceous-paleogene accretion. *Geodinamica Acta*, *10*(4), 137-157.
Gebauer, D., Schertl, H.-P., Brix, M., & Schreyer, W. (1997). 35 ma old ultrahigh-pressure metamorphism and evidence for very rapid exhumation in the dora maira massif, western alps. *Lithos*, *41*(1-3), 5-24.
Gerya, T. V., Stöckhert, B., & Perchuk, A. L. (2002). Exhumation of high-pressure metamorphic rocks in a subduction channel: A numerical simulation. *Tectonics*, *21*(6), 6-1-6-19.
Gerya, T. V., & Yuen, D. A. (2003). Characteristics-based marker-in-cell method with conservative finite-differences schemes for modeling geological flows with strongly variable transport properties. *Physics of the Earth and Planetary Interiors*, *140*(4), 293–318.
Ghent, E. (2020). Metamorphic facies: A review and some suggestions for changes. *The Canadian Mineralogist*, *58*(4), 437-444.
Gianola, O., Schmidt, M. W., von Quadt, A., Peytcheva, I., Luraschi, P., & Reusser, E. (2014). Continuity in geochemistry and time of the tertiary bergell intrusion (central alps). *Swiss Journal of Geosciences*, *107*(2), 197-222.
Goffé, B., & Bousquet, R. (1997). Ferrocarpholite, chloritoid and lawsonite in metapelites of the versoyen and petit st bernard units (valais zone, western alps). *Schweizerische Mineralogische und Petrographische Mitteilungen*, *77*(2), 137-147.
Gregory, C. J., McFarlane, C. R., Hermann, J., & Rubatto, D. (2009). Tracing the evolution of calc-alkaline magmas: in-situ sm–nd isotope studies of accessory minerals in the bergell igneous complex, italy. *Chemical Geology*, *260*(1-2), 73-86.
Groppo, C., Ferrando, S., Gilio, M., Botta, S., Nosenzo, F., Balestro, G., ... Rolfo, F. (2019). What's in the sandwich? new p–t constraints for the (u) hp nappe stack of southern dora-maira massif (western alps). *European Journal of Mineralogy*, *31*(4), 665-683.
Guillot, S., Schwartz, S., Reynard, B., Agard, P., & Prigent, C. (2015). Tectonic significance of serpentinites. *Tectonophysics*, *646*, 1-19.
Hacker, B. R., & Gerya, T. V. (2013). Paradigms, new and old, for ultrahigh-pressure tectonism. *Tectonophysics*, *603*, 79-88.
Inger, S., Ramsbotham, W., Cliff, R., & Rex, D. (1996). Metamorphic evolution of the sesia-lanzo zone, western alps: time constraints from multi-system geochronology. *Contributions to Mineralogy and Petrology*, *126*(1-2), 152-168.

Isacks, B., Oliver, J., & Sykes, L. R. (1968). Seismology and the new global tectonics. *Journal of Geophysical Research*, *73*(18), 5855-5899.

Jamieson, R. A., Beaumont, C., Fullsack, P., & Lee, B. (1998). Barrovian regional metamorphism: Where's the heat? *Geological Society, London, Special Publications*, *138*(1), 23-51.

Keller, L. M., Hess, M., Fügenschuh, B., & Schmid, S. M. (2005). Structural and metamorphic evolution of the camughera–moncucco, antrona and monte rosa units southwest of the simplon line, western alps. *Eclogae Geologicae Helvetiae*, *98*(1), 19-49.

Kiss, D., Candioti, L. G., Duretz, T., & Schmalholz, S. M. (2020). Thermal softening induced subduction initiation at a passive margin. *Geophysical Journal International*, *220*(3), 2068-2073.

Kiss, D., Podladchikov, Y., Duretz, T., & Schmalholz, S. M. (2019). Spontaneous generation of ductile shear zones by thermal softening: Localization criterion, 1d to 3d modelling and application to the lithosphere. *Earth and Planetary Science Letters*, *519*, 284-296.

Kurz, W., & Froitzheim, N. (2002). The exhumation of eclogite-facies metamorphic rocks—a review of models confronted with examples from the alps. *International Geology Review*, *44*(8), 702-743.

Lardeaux, J.-M. (2014). Deciphering orogeny: a metamorphic perspective. examples from european alpine and variscan belts: Part i: Alpine metamorphism in the western alps. a review. *Bulletin de la Société Géologique de France*, *185*(2), 93-114.

Lardeaux, J.-M., & JM, L. (1982). Relations entre le metamorphisme et la deformation dans la zone sesia-lanzo (alpes occidentales) et le probleme de l'eclogitisation de la croute continentale.

Lemoine, M., Bas, T., Arnaud-Vanneau, A., Arnaud, H., Dumont, T., Gidon, M., ... Megard-Galli, J. (1986). The continental margin of the mesozoic tethys in the western alps. *Marine and petroleum geology*, *3*(3), 179-199.

Le Pichon, X. (1968). Sea-floor spreading and continental drift. *Journal of Geophysical Research*, *73*(12), 3661-3697.

Liati, A., Gebauer, D., & Fanning, C. M. (2009). Geochronological evolution of hp metamorphic rocks of the adula nappe, central alps, in pre-alpine and alpine subduction cycles. *Journal of the Geological Society*, *166*(4), 797-810.

Luisier, C., Baumgartner, L., Schmalholz, S. M., Siron, G., & Vennemann, T. (2019). Metamorphic pressure variation in a coherent alpine nappe challenges lithostatic pressure paradigm. *Nature communications*, *10*(1), 1-11.

Malusà, M. G., Guillot, S., Zhao, L., Paul, A., Solarino, S., Dumont, T., ... Eva, E. (2021). The deep structure of the alps based on the cifalps seismic experiment: A synthesis. *Geochemistry, Geophysics, Geosystems*, *22*(3), e2020GC009466.

Mancktelow, N. (1985). The simplon line: a major displacement zone in the western lepontine alps. *Eclogae Geologicae Helvetiae*, *78*(1), 73-96.

Manzotti, P., Ballevre, M., Zucali, M., Robyr, M., & Engi, M. (2014). The tectonometamorphic evolution of the sesia–dent blanche nappes (internal western alps): review and synthesis. *Swiss Journal of Geosciences*, *107*(2), 309–336.

Manzotti, P., Bosse, V., Pitra, P., Robyr, M., Schiavi, F., & Ballevre, M. (2018). Exhumation rates in the gran paradiso massif (western alps) constrained by in situ u–th–pb dating of accessory phases (monazite, allanite and xenotime). *Contributions to Mineralogy and Petrology*, *173*(3), 24.

Manzotti, P., Zucali, M., Ballevre, M., Robyr, M., & Engi, M. (2014). Geometry and kinematics of the roisan-cignana shear zone, and the orogenic evolution of the dent blanche tectonic system (western alps). *Swiss Journal of Geosciences*, *107*(1), 23–47.

McCarthy, A., Tugend, J., Mohn, G., Candioti, L., Chelle-Michou, C., Arculus, R.,

. . . Müntener, O. (2020). A case of ampferer-type subduction and consequences for the alps and the pyrenees. *American Journal of Science*, *320*(4), 313-372.

Miyashiro, A. (2012). *Metamorphism and metamorphic belts.* Springer Science & Business Media.

Morgan, W. J. (1968). Rises, trenches, great faults, and crustal blocks. *Journal of Geophysical Research*, *73*(6), 1959-1982.

Oberhänsli, R., Bousquet, R., Engi, M., Goffé, B., Gosso, G., Handy, M., . . . Polino, R. (2004). Metamorphic structure of the alps. *CCGM (Commission of the Geological Maps of the World), Paris.*.

Oberli, F., Meier, M., Berger, A., Rosenberg, C. L., & GierÉ, R. (2004). U-th-pb and 230th/238u disequilibrium isotope systematics: Precise accessory mineral chronology and melt evolution tracing in the alpine bergell intrusion. *Geochimica et Cosmochimica Acta*, *68*(11), 2543-2560.

Palin, R. M., Santosh, M., Cao, W., Li, S.-S., Hernández-Uribe, D., & Parsons, A. (2020). Secular metamorphic change and the onset of plate tectonics. *Earth-Science Reviews*, 103172.

Philpotts, A., & Ague, J. (2009). *Principles of igneous and metamorphic petrology.* Cambridge University Press.

Poh, J., Yamato, P., Duretz, T., Gapais, D., & Ledru, P. (2020). Precambrian deformation belts in compressive tectonic regimes: A numerical perspective. *Tectonophysics*, *777*, 228350.

Reddy, S., Wheeler, J., & Cliff, R. (1999). The geometry and timing of orogenic extension: an example from the western italian alps. *Journal of Metamorphic Geology*, *17*, 573-590.

Reddy, S. M., Wheeler, J., Butler, R. W. H., Cliff, R. A., Freeman, S., Inger, S., . . . Kelley, S. P. (2003). Kinematic reworking and exhumation within the convergent alpine orogen. *Tectonophysics*, *365*(1-4), 77-102.

Reinecke, T. (1991). Very-high-pressure metamorphism and uplift of coesite-bearing metasediments from the zermatt-saas zone, western alps. *European Journal of Mineralogy*, 7-18.

Ring, U., & Merle, O. (1992). Forethrusting, backfolding, and lateral gravitational escape in the northern part of the western alps (monte rosa region). *Geological Society of America Bulletin*, *104*(7), 901-914.

Rubatto, D., Gebauer, D., & Compagnoni, R. (1999). Dating of eclogite-facies zircons: the age of alpine metamorphism in the sesia–lanzo zone (western alps). *Earth and Planetary Science Letters*, *167*(3-4), 141-158.

Rubatto, D., & Hermann, J. (2001). Exhumation as fast as subduction? *Geology*, *29*(1), 3-6.

Ruh, J. B., Le Pourhiet, L., Agard, P., Burov, E., & Gerya, T. (2015). Tectonic slicing of subducting oceanic crust along plate interfaces: Numerical modeling. *Geochemistry, Geophysics, Geosystems*, *16*(10), 3505-3531.

Ryan, P. D., & Dewey, J. F. (2019). The sources of metamorphic heat during collisional orogeny: The barrovian enigma. *Canadian Journal of Earth Sciences*, *56*(12), 1309-1317.

Saliot, P. (1973). Principal zones of metamorphism in french-alps-distribution and significance. *COMPTES RENDUS HEBDOMADAIRES DES SEANCES DE L ACADEMIE DES SCIENCES SERIE D*, *276*(24), 3081-&.

Schenker, F. L., Schmalholz, S. M., Moulas, E., Pleuger, J., Baumgartner, L. P., Podladchikov, Y., . . . Müntener, O. (2015). Current challenges for explaining (ultra) high-pressure tectonism in the pennine domain of the central and western alps. *Journal of Metamorphic Geology*, *33*(8), 869-886.

Schlunegger, F., & Willett, S. (1999). Spatial and temporal variations in exhumation of the central swiss alps and implications for exhumation mechanisms. *Geological Society, London, Special Publications*, *154*(1), 157-179.

Schmalholz, S. M., & Schenker, F. L. (2016). Exhumation of the dora maira ultrahigh-pressure unit by buoyant uprise within a low-viscosity mantle oblique-slip shear zone. *Terra Nova*, *28*(5), 348-355.
Schmid, S., & Kissling, E. (2000). The arc of the western alps in the light of geophysical data on deep crustal structure. *Tectonics*, *19*(1), 62-85.
Schmid, S. M., Fügenschuh, B., Kissling, E., & Schuster, R. (2004). Tectonic map and overall architecture of the alpine orogen. *Eclogae Geologicae Helvetiae*, *97*(1), 93-117.
Schmid, S. M., Kissling, E., Diehl, T., van Hinsbergen, D. J., & Molli, G. (2017). Ivrea mantle wedge, arc of the western alps, and kinematic evolution of the alps–apennines orogenic system. *Swiss Journal of Geosciences*, *110*(2), 581-612.
Schwartz, S., Allemand, P., & Guillot, S. (2001). Numerical model of the effect of serpentinites on the exhumation of eclogitic rocks: insights from the monviso ophiolitic massif (western alps). *Tectonophysics*, *342*(1-2), 193-206.
Spear, F. S. (1989). Petrologic determination of metamorphic pressure-temperature-time paths. *Metamorphic Pressure-Temperature-Time Paths*, *7*, 1-55.
Spear, F. S., Pattison, D. R., & Cheney, J. T. (2017). The metamorphosis of metamorphic petrology. *The Web of Geological Sciences: Advances, Impacts, and Interactions II, Geol. Soc. Am*, *523*, 31-73.
Steck, A., & Hunziker, J. (1994). The tertiary structural and thermal evolution of the central alps—compressional and extensional structures in an orogenic belt. *Tectonophysics*, *238*(1-4), 229-254.
Steck, A., Masson, H., & Robyr, M. (2015). Tectonics of the monte rosa and surrounding nappes (switzerland and italy): Tertiary phases of subduction, thrusting and folding in the pennine alps. *Swiss Journal of Geosciences*, *108*(1), 3-34.
Stöckhert, B., & Gerya, T. V. (2005). Pre-collisional high pressure metamorphism and nappe tectonics at active continental margins: A numerical simulation. *Terra Nova*, *17*(2), 102-110.
Stüwe, K. (1998). Heat sources of cretaceous metamorphism in the eastern alps—a discussion. *Tectonophysics*, *287*(1-4), 251-269.
Thompson, A. (1984). Geothermal gradients through time. In *Patterns of change in earth evolution* (pp. 345–355).
Tilton, G., Schreyer, W., & Schertl, H.-P. (1989). Pb-sr-nd isotopic behavior of deeply subducted crustal rocks from the dora maira massif, western alps, italy. *Geochimica et Cosmochimica Acta*, *53*(6), 1391-1400.
Trümpy, R. (1975). Penninic-austroalpine boundary in the swiss alps: a presumed former continental margin and its problems. *American Journal of Science*, *275*(A), 209-238.
Vaughan-Hammon, J. D., Luisier, C., Baumgartner, L. P., & Schmalholz, S. M. (2021). Peak alpine metamorphic conditions from staurolite bearing metapelites in the monte rosa nappe (central european alps) and geodynamic implications. *Journal of Metamorphic Geology*.
von Blackenburg, F. (1992). Combined high-precision chronometry and geochemical tracing using accessory minerals: applied to the central-alpine bergell intrusion (central europe). *Chemical Geology*, *100*(1-2), 19-40.
Vuichard, J., & Ballevre, M. (1988). Garnet–chloritoid equilibria in eclogitic pelitic rocks from the sesia zone (western alps): their bearing on phase relations in high pressure metapelites. *Journal of metamorphic Geology*, *6*(2), 135-157.
Warren, C. (2013). Exhumation of (ultra-) high-pressure terranes: concepts and mechanisms. *Solid Earth*, *4*(1), 75-92.
Warren, C., Beaumont, C., & Jamieson, R. A. (2008). Modelling tectonic styles and ultra-high pressure (uhp) rock exhumation during the transition from oceanic subduction to continental collision. *Earth and Planetary Science Letters*,

267(1-2), 129-145.
Wheeler, J., Reddy, S., & Cliff, R. (2001). Kinematic linkage between internal zone extension and shortening in more external units in the nw alps. *Journal of the Geological Society*, *158*(3), 439-443.
Wiederkehr, M., Bousquet, R., Schmid, S. M., & Berger, A. (2008). From subduction to collision: thermal overprint of hp/lt meta-sediments in the north-eastern lepontine dome (swiss alps) and consequences regarding the tectono-metamorphic evolution of the alpine orogenic wedge. *Swiss Journal of Geosciences*, *101*(1), 127-155.
Wiederkehr, M., Bousquet, R., Ziemann, M., Schmid, S., & Berger, A. (2007). Thermal structure of the valaisan and ultra-helvetic sedimentary units of the northern lepontine dome—consequences regarding the tectono-metamorphic evolution. *EGU, Wien*.
Wilson, J. T. (1966). Did the atlantic close and then re-open?
Yamato, P., Agard, P., Burov, E., Le Pourhiet, L., Jolivet, L., & Tiberi, C. (2007). Burial and exhumation in a subduction wedge: Mutual constraints from thermomechanical modeling and natural p-t-t data (schistes lustrés, western alps). *Journal of Geophysical Research: Solid Earth*, *112*(B7).
Yamato, P., Burov, E., Agard, P., Le Pourhiet, L., & Jolivet, L. (2008). Hp-uhp exhumation during slow continental subduction: Self-consistent thermodynamically and thermomechanically coupled model with application to the western alps. *Earth and Planetary Science Letters*, *271*(1-4), 63-74.
Yang, J., Lu, G., Liu, T., Li, Y., Wang, K., Wang, X., ... Zhao, L. (2020). Amagmatic subduction produced by mantle serpentinization and oceanic crust delamination. *Geophysical Research Letters*, *47*(9), e2019GL086257.

Supporting Information for "Metamorphic facies evolution and distribution in the Western Alps predicted by numerical modelling"

Joshua D. Vaughan-Hammon[1], Lorenzo G. Candioti[1], Thibault Duretz[2],

Stefan M. Schmalholz[1]

[1]Institut des sciences de la Terre, Bâtiment Géopolis, Quartier UNIL-Mouline, Université de Lausanne, 1015 Lausanne (VD), Switzerland

[2]Univ Rennes, CNRS, Géosciences Rennes UMR 6118, Rennes, France

Contents of this file

1. Algorithm description
2. Figures S1 to S2
3. Table S1

Additional Supporting Information (Files uploaded separately)

1. Caption for large Table S2

Introduction

The supporting information contains a detailed description of the numerical algorithm used, the modelling approach and the initial model configuration used in this study.

Algorithm description

As common in continuum mechanics, we solve the thermomechanically coupled equations for continuity of material, conservation of momentum and energy expressed w.r.t temperature, T, as

$$\frac{\partial v_i}{\partial x_i} = 0 \tag{1}$$

$$\frac{\partial \sigma_{ij}}{\partial x_j} = -\rho \; g_i \tag{2}$$

$$\rho \; c_\mathrm{P} \; \frac{\mathrm{D}T}{\mathrm{D}t} = \frac{\partial}{\partial x_i}\left(k \, \frac{\partial T}{\partial x_i}\right) + H_\mathrm{A} + H_\mathrm{D} + H_\mathrm{R} \; , \tag{3}$$

where v is velocity, x is the coordinate, i and j indicate the horizontal (j,j=1) or vertical (i,j=2) direction, ρ denotes density, $g_i = \left[0; -9.81\right]$ are the components of the gravitational acceleration vector, c_P is heat capacity, k is thermal conductivity, $\frac{\mathrm{D}}{\mathrm{D}t}$ is the material time derivative, H_A, H_D and H_R are contributions resulting from adiabatic processes, viscoplastic dissipation and radiogenic heat production, respectively. We here employ the extended Boussinesq approximation, i.e. the slowly flowing fluid is considered to be incompressible, density changes are only taken into account when multiplied with gravitational acceleration and adiabatic processes only impact on temperature (Candioti et al., 2020). The total stress tensor components are defined as

$$\sigma_{ij} = -P\delta_{ij} + 2 \; \eta^\mathrm{eff} \; \dot{\varepsilon}_{ij}^\mathrm{eff} \; , \tag{4}$$

where $\delta_{ij} = 0$ if $i \neq j$, or $\delta_{ij} = 1$ if $i = j$, η^eff is the effective viscosity, $\dot{\varepsilon}_{ij}^\mathrm{eff}$ are the components of the effective deviatoric strain rate tensor,

$$\dot{\varepsilon}_{ij}^\mathrm{eff} = \left(\dot{\varepsilon}_{ij} + \frac{\tau_{ij}^o}{2G\Delta t}\right) \; , \tag{5}$$

where G is the shear modulus, Δt is the time step and τ_{ij}^{o} are the deviatoric stress tensor components of the preceding time step. We consider visco–elasto–plastic rheologies by additive decomposition (Maxwell model) of the total deviatoric strain rate tensor components $\dot{\varepsilon}_{\mathrm{ij}}$ into contributions from the viscous (dislocation, diffusion and Peierls creep), plastic and elastic deformation as

$$\dot{\varepsilon}_{ij} = \dot{\varepsilon}_{ij}^{\mathrm{ela}} + \dot{\varepsilon}_{ij}^{\mathrm{pla}} + \dot{\varepsilon}_{ij}^{\mathrm{dis}} + \dot{\varepsilon}_{ij}^{\mathrm{dif}} + \dot{\varepsilon}_{ij}^{\mathrm{pei}} \ . \tag{6}$$

Furthermore, we perform an iteration cycle locally on each grid cell until Eq. 6 is satisfied (e.g., Popov & Sobolev, 2008). The effective viscosity for the dislocation and Peierls creep flow law is a function of the second invariant of the respective strain rate components $\dot{\varepsilon}_{\mathrm{II}}^{\mathrm{dis,pei}} = \tau_{\mathrm{II}}/(2\eta^{\mathrm{dis,pei}})$

$$\eta^{\mathrm{dis}} = \frac{2^{\frac{1-n}{n}}}{3^{\frac{1+n}{2n}}} \ \zeta \ A^{-\frac{1}{n}} \ \left(\dot{\varepsilon}_{\mathrm{II}}^{\mathrm{dis}}\right)^{\frac{1}{n}-1} \ \exp\left(\frac{Q+PV}{nRT}\right) \ \left(f_{\mathrm{H_2O}}\right)^{-\frac{r}{n}} \ , \tag{7}$$

where the ratio in front of the pre-factor ζ is a correction factor (e.g., Schmalholz & Fletcher, 2011). A, n, Q, V, $f_{\mathrm{H_2O}}$ and r are material parameters determined in laboratory experiments. Diffusion creep is taken into account for the mantle material and its viscosity is defined as

$$\eta^{\mathrm{dif}} = \frac{1}{3} \ A^{-1} \ d^{m} \ \exp\left(\frac{Q+PV}{RT}\right) \ \left(f_{\mathrm{H_2O}}\right)^{-r}, \tag{8}$$

where d is grain size and m is a grain size exponent. Effective Peierls viscosity is calculated using the experimentally derived flow law by (Goetze & Evans, 1979) in the regularised form (Kameyama et al., 1999) as

$$\eta^{\mathrm{pei}} = \frac{2^{\frac{1-s}{s}}}{3^{\frac{1+s}{2s}}} \; \hat{A} \; \left(\dot{\varepsilon}_{\mathrm{II}}^{\mathrm{pei}}\right)^{\frac{1}{s}-1} \; , \tag{9}$$

where s is a stress exponent:

$$s = 2 \; \gamma \; \frac{Q}{RT} (1-\gamma) \; . \tag{10}$$

$\hat{A}$ in Eq. (9) is

$$\hat{A} = \left[A_{\mathrm{P}} \; \exp\left(- \frac{Q(1-\gamma)^2}{RT} \right) \right]^{-\frac{1}{s}} \; \gamma \sigma_{\mathrm{P}} \; , \tag{11}$$

where A_{P} is a pre-factor, γ is a fitting parameter and σ_{P} is a characteristic stress value. Brittle-plastic failure is included by limiting the stresses by a Drucker-Prager yield function

$$F = \tau_{\mathrm{II}} - P \; \sin\phi - C \; \cos\phi \; , \tag{12}$$

where ϕ is the internal angle of friction and C is the cohesion. In case the yield condition is met ($F \geq 0$), the equivalent plastic viscosity is computed as

$$\eta^{\mathrm{pla}} = \frac{P \; \sin\phi + C \; \cos\phi}{2\dot{\varepsilon}_{\mathrm{II}}^{\mathrm{eff}}} \tag{13}$$

and the effective deviatoric strain rate is equal to the plastic contribution of the deviatoric strain rate (Eq. 5). At the end of the iteration cycle, the effective viscosity in Eq. 4 is either computed as the quasi-harmonic average of the viscoelastic contributions

$$\eta^{\mathrm{eff}} = \begin{cases} \left(\frac{1}{G\Delta t} + \frac{1}{\eta^{\mathrm{dis}}} + \frac{1}{\eta^{\mathrm{dif}}} + \frac{1}{\eta^{\mathrm{pei}}} \right)^{-1} & , \; F < 0 \\ \eta^{\mathrm{pla}} & , \; F \geq 0 \end{cases} \tag{14}$$

or is equal to the viscosity η^{pla} calculated at the yield stress according to Eq. 13. Rigid body rotation is computed analytically at the end of each time step as

$$
\begin{aligned}
\tau_{ij} &= \mathbf{R}^{\mathbf{T}}\, \tau_{ij}\, \mathbf{R}\ , && (15)\\
\mathbf{R} &= \begin{bmatrix} \cos\theta & -\sin\theta \\ \sin\theta & \cos\theta \end{bmatrix}, && (16)\\
\theta &= \Delta t\, \omega_{ij}\ , && (17)\\
\omega_{ij} &= \frac{1}{2}\left(\frac{\partial v_j}{\partial x_i} - \frac{\partial v_i}{\partial x_j}\right), && (18)\\
& && (19)
\end{aligned}
$$

where $\mathbf{R}$ is the rotation matrix, $^{\mathbf{T}}$ is the transpose operator, θ is the rotation angle and ω_{ij} are components of the vorticity tensor.

Data Set S1.

Movie S1.

Audio S1.

References

Candioti, L. G., Schmalholz, S. M., & Duretz, T. (2020). Impact of upper mantle convection on lithosphere hyperextension and subsequent horizontally forced subduction initiation. *Solid Earth*, *11*(6), 2327-2357.

Goetze, C., & Evans, B. (1979). Stress and temperature in the bending lithosphere as constrained by experimental rock mechanics. *Geophysical Journal International*, *59*(3), 463–478.

Hansen, F., & Carter, N. (1983). Semibrittle creep of dry and wet westerly granite at 1000 mpa. In *The 24th us symposium on rock mechanics (usrms).*

Hilairet, N., Reynard, B., Wang, Y., Daniel, I., Merkel, S., Nishiyama, N., & Petitgirard, S. (2007). High-pressure creep of serpentine, interseismic deformation, and initiation of subduction. *Science*, *318*(5858), 1910–1913.

Hirth, G., & Kohlstedt, D. (2003). Rheology of the upper mantle and the mantle wedge: A view from the experimentalists. *Geophysical Monograph-American Geophysical Union*, *138*, 83–106.

Holland, T., & Powell, R. (1998). An internally consistent thermodynamic data set for phases of petrological interest. *Journal of metamorphic Geology*, *16*(3), 309–343.

Kameyama, M., Yuen, D. A., & Karato, S.-I. (1999). Thermal-mechanical effects of low-temperature plasticity (the peierls mechanism) on the deformation of a viscoelastic shear zone. *Earth and Planetary Science Letters*, *168*(1-2), 159–172.

Kronenberg, A. K., Kirby, S. H., & Pinkston, J. (1990). Basal slip and mechanical anisotropy of biotite. *Journal of Geophysical Research: Solid Earth*, *95*(B12), 19257–19278.

Mackwell, S., Zimmerman, M., & Kohlstedt, D. (1998). High-temperature deformation of dry diabase with application to tectonics on venus. *Journal of Geophysical Research: Solid Earth*, *103*(B1), 975–984.

Pelletier, L., Müntener, O., Kalt, A., Vennemann, T. W., & Belgya, T. (2008). Emplacement of ultramafic rocks into the continental crust monitored by light and other trace elements: An example from the geisspfad body (swiss-italian alps). *Chemical Geology*, *255*(1-2), 143–159.

Philpotts, A., & Ague, J. (2009). *Principles of igneous and metamorphic petrology.* Cambridge University Press.

Popov, A., & Sobolev, S. V. (2008). Slim3d: A tool for three-dimensional thermomechanical modeling of lithospheric deformation with elasto-visco-plastic rheology. *Physics of the earth and planetary interiors*, *171*(1-4), 55–75.

Ranalli, G. (1995). *Rheology of the earth.* Springer Science & Business Media.

Rybacki, E., & Dresen, G. (2004). Deformation mechanism maps for feldspar rocks. *Tectonophysics*, *382*(3-4), 173–187.

Schmalholz, S. M., & Fletcher, R. C. (2011). The exponential flow law applied to necking and folding of a ductile layer. *Geophysical Journal International*, *184*(1), 83–89.

Schmid, S., Boland, J., & Paterson, M. (1977). Superplastic flow in finegrained limestone. *Tectonophysics*, *43*(3-4), 257–291.

Stixrude, L., & Lithgow-Bertelloni, C. (2011). Thermodynamics of mantle minerals-ii. phase equilibria. *Geophysical Journal International*, *184*(3), 1180–1213.

Winter, J. D. (2013). *Principles of igneous and metamorphic petrology.* Pearson education.

Workman, R. K., & Hart, S. R. (2005). Major and trace element composition of the depleted morb mantle (dmm). *Earth and Planetary Science Letters*, *231*(1-2), 53–72.

pdf/FIG_S1_IniConf.pdf

Figure S1. **a** & **d** Velocity boundary condition values defined at the western and eastern boundary. Duration of deformation periods as follows: extension = 50 Myr, no deformation = 60 Myr, convergence = 30 Myr with 1.5 cm yr^{-1} and 1.0 cm yr^{-1} until the end of the simulation. **b** Entire model domain, initial thermal profile and mechanical boundary conditions at the top and bottom boundary. White to red colour is the viscosity field in the mantle calculated by the numerical algorithm and yellow to orange and green colours are the upper and lower crust, respectively. Rheological parameters used for crustal matrix = Wet Anorthite with weakening prefactor 0.3 during extension and cooling, Westerly Granite during convergence; lithosphere and upper mantle = Strong mantle, elliptical inclusions in the lithosphere = Weak mantle. Material parameters for all phases as indicated in Table S1. **c** Enlargement of the domain centre. Colouring in all subplots as indicated in the figure legend.

pdf/FIG_S2_maxPT.pdf

Figure S2. Numerical metamorphic facies variability using maximum pressure or maximum temperature. Pressure-temperature evolution of numerical marker with tectonic pressure (solid black line) compared to marker of close proximity, without significant tectonic pressure (dashed black line). **a** Temperature evolution through time. **b** Pressure evolution through time. **c** Pressure-temperature evolution overlaying metamorphic facies grid (adapted from Philpotts & Ague, 2009) indicating disparity of predicted metamorphic facies for solid black line marker, using maximum pressure (blueschist) or maximum temperature (greenschist).

Table S1. Physical parameters used in the numerical simulations.

Model unit	Rheology (Reference)		k [W m^{-1} K^{-1}]	H_R [W m^{-3}]	C [Pa]	φ [°]
Crustal matrix 1[*,a]	Wet Anorthite (Rybacki & Dresen, 2004)		2.25	1.0200×10^{-6}	1×10^{7}	30
Crustal matrix 2[*,a]	Westerly Granite (Hansen & Carter, 1983)		2.25	1.0200×10^{-6}	1×10^{7}	30
Weak inclusion[*,a]	Wet Quartzite (Ranalli, 1995)		2.25	1.0200×10^{-6}	1×10^{6}	5
Strong inclusion[*,a]	Maryland Diabase (Mackwell et al., 1998)		2.25	1.0200×10^{-6}	1×10^{7}	30
Calcite[*,a]	Calcite (Schmid et al., 1977)		2.37	0.5600×10^{-6}	1×10^{7}	30
Mica[*,a]	Mica (Kronenberg et al., 1990)		2.55	2.9000×10^{-6}	1×10^{7}	15
Lower crust[*,b]	Wet Anorthite (Rybacki & Dresen, 2004)		2.25	0.2600×10^{-6}	1×10^{7}	30
Strong mantle[*,c]	Dry Olivine (Hirth & Kohlstedt, 2003)		2.75	2.1139×10^{-8}	1×10^{7}	30
Weak mantle[*,c]	Wet Olivine (Hirth & Kohlstedt, 2003)		2.75	2.1139×10^{-8}	1×10^{7}	30
Serpentinite[*,d]	Antigorite (Hilairet et al., 2007)		2.75	2.1139×10^{-8}	1×10^{7}	25
Dislocation creep	A [Pa^{-n-r} s^{-1}]	ζ [ ]	n [ ]	Q [J mol^{-1}]	V [m^3 mol^{-1}]	r [ ]
Crustal matrix 1	3.9811×10^{-16}	0.3[e], 1.0	3.0	356×10^{3}	0.00×10^{-6}	0.0
Crustal matrix 2	3.1623×10^{-26}	1.0	3.3	186.5×10^{3}	0.00×10^{-6}	0.0
Weak inclusion	5.0717×10^{-18}	1.0	2.3	154×10^{3}	0.00×10^{-6}	0.0
Strong inclusion	5.0477×10^{-28}	1.0	4.7	485×10^{3}	0.00×10^{-6}	0.0
Calcite	1.5849×10^{-25}	1.0	4.7	297×10^{3}	0.00×10^{-6}	0.0
Mica	1.0000×10^{-138}	1.0	18.0	51.0×10^{3}	0.00×10^{-6}	0.0
Lower crust	3.9811×10^{-16}	1.0	3.0	356×10^{3}	0.00×10^{-6}	0.0
Strong mantle	1.1000×10^{-16}	1.0	3.5	530×10^{3}	14.0×10^{-6}	0.0
Weak mantle[1]	5.6786×10^{-27}	1.0	3.5	480×10^{3}	11.0×10^{-6}	1.2
Serpentinite	4.4738×10^{-38}	1.0	3.8	8.90×10^{3}	3.20×10^{-6}	0.0
Diffusion creep[2]	A [Pa^{-n-r} m^{m} s^{-1}]	m [ ]	n [ ]	Q [J mol^{-1}]	V [m^3 mol^{-1}]	r [ ]
Strong mantle	1.5000×10^{-15}	3.0	1.0	370×10^{3}	7.5×10^{-6}	0.0
Weak mantle[1]	2.5000×10^{-23}	3.0	1.0	375×10^{3}	9.0×10^{-6}	1.0
Peierls creep	A_P [s^{-1}]	Q [J mol^{-1}]	V [m^3 mol^{-1}]	σ_P [Pa]	γ [ ]	
Mantle[3]	5.7000×10^{11}	540×10^{3}	0.0×10^{-6}	8.5×10^{9}	0.1	

[*] $c_P = 1050$ [J kg^{-1} K^{-1}]

[a] $G = 2\times10^{10}$ [Pa], $\rho_0 = 2800$ [kg m^{-3}],$\alpha = 3.5\times10^{-5}$ [K^{-1}], $\beta = 1\times10^{-11}$ [Pa^{-1}]

[b] $G = 2\times10^{10}$ [Pa], $\rho_0 = 2900$ [kg m^{-3}],$\alpha = 3.5\times10^{-5}$ [K^{-1}], $\beta = 1\times10^{-11}$ [Pa^{-1}]

[c] $G = 2\times10^{10}$ [Pa]

[d] $G = 1.81\times10^{10}$ [Pa], $\rho_0 = 2585$ [kg m^{-3}],$\alpha = 4.7\times10^{-5}$ [K^{-1}], $\beta = 1\times10^{-11}$ [Pa^{-1}]

[e] Weakening prefactor employed during extension and cooling.

[1] A water fugacity $f_{\mathrm{H_2O}} = 1.0\times10^{9}$ [Pa] is used. For all other phases $f_{\mathrm{H_2O}}$= 0.0 [Pa].

[2] A constant grain size $d = 1\times10^{-3}$ [m] is used.

[3] Reference: (Goetze & Evans, 1979) regularized by (Kameyama et al., 1999)

Table S2. Bulk rock composition and solution models used for phase equilibrium modelling

[1] Bulk rock modified after (Winter, 2013)

[2] Bulk rock modified after (Pelletier et al., 2008)

[3] Bulk rock modified after (Workman & Hart, 2005). We assume water saturation in all calculations. Crosses denote solution models used for given lithologies.

[4] Thermodynamic database: (Holland & Powell, 1998) updated in 2002

[5] Thermodynamic database: (Stixrude & Lithgow-Bertelloni, 2011) for depleted MORB mantle (DMM). Details on the solution models can be found in the solution_model.dat data file in Perple_X.

Oxides [wt%]	Pelite (avg.)[1,4]	Rhyolite[1,4]	Andesite[1,4]	MORB[1,4]	Hydrated Peridote[1,4]	Serpentinite[2,4]	Bulk DMM[3,5]
SiO_2	61.5	72.8	57.9	49.2	44.71	44.21	44.71
Al_2O_3	18.6	13.3	17	16.1	4.16	3.13	3.98
FeO	10	2.44	6.98	10.22	8.07	8.898	8.18
MgO	3.81	0.39	3.33	6.44	39.2	39.24	38.73
CaO	-	-	6.79	10.5	2.42	3.06	3.17
Na_2O	1.46	3.55	3.48	3.01	0.22	-	0.13
K_2O	3.02	4.3	1.62	1.1	-	-	-
H_20	sat	sat	sat	sat	sat	sat	-
Solution models							
Opx(HP)	+	+	+	+	+	+	-
Gt(GCT)	+	+	+	+	+	+	-
feldspar	+	+	+	+	+	+	-
Chl(HP)	+	+	+	+	+	+	-
Sp(HP)	+	+	+	+	+	+	-
O(HP)	+	+	+	+	+	+	-
Stlp(M)	+	+	+	+	-	-	-
Carp	+	+	+	+	-	-	-
Sud	+	+	+	+	-	-	-
Bio(TCC)	+	+	+	+	-	-	-
St(HP)	+	+	+	+	-	-	-
Ctd(HP)	+	+	+	+	-	-	-
Pheng(HP)	+	+	+	+	-	-	-
hCrd	+	+	+	+	+	+	-
Omph	-	-	+	+	+	+	-
GlTrTsPg	-	-	+	+	+	+	-
Pu(M)	-	-	+	+	+	-	-
Act(M)	-	-	+	+	+	+	-
T	-	-	+	-	+	+	-
A-phase	-	-	-	-	+	+	-
Chum	-	-	-	-	+	+	-
B	-	-	-	-	+	+	-
Wus	-	-	-	-	+	+	-
Fperh	-	-	-	-	+	+	-
Atg(PN)	-	-	-	-	+	+	-
Bulk DMM							
C2/c	-	-	-	-	-	-	+
Wus	-	-	-	-	-	-	+
Pv	-	-	-	-	-	-	+
Pl	-	-	-	-	-	-	+
Sp	-	-	-	-	-	-	+
O	-	-	-	-	-	-	+
Wad	-	-	-	-	-	-	+
Ring	-	-	-	-	-	-	+
Opx	-	-	-	-	-	-	+
Cpx	-	-	-	-	-	-	+
Aki	-	-	-	-	-	-	+
Gt_maj	-	-	-	-	-	-	+
Ppv	-	-	-	-	-	-	+
CF	-	-	-	-	-	-	+

Explanation and References
sat = saturation
[1]Winter 2013
[2]Pelletier 2008
[3]Workman & Hart 2005
[4]Holland and Powell 1998, updated in 2002
[5]Stixrude 2011
Full references given in supplementary material